Sediment disturbance due to storm wave action on a steep, mixed sand and gravel beach on the Bay of Fundy

by

Winson Li

Submitted in partial fulfilment of the requirements for the degree of
Combined Honours Bachelor of Science in Earth Sciences and Oceanography

at

Dalhousie University
Halifax, Nova Scotia
April, 2015

Revised February 3, 2017

Distribution License

DalSpace requires agreement to this non-exclusive distribution license before your item can appear on DalSpace.

NON-EXCLUSIVE DISTRIBUTION LICENSE

You (the author(s) or copyright owner) grant to Dalhousie University the non-exclusive right to reproduce and distribute your submission worldwide in any medium.

You agree that Dalhousie University may, without changing the content, reformat the submission for the purpose of preservation.

You also agree that Dalhousie University may keep more than one copy of this submission for purposes of security, back-up and preservation.

You agree that the submission is your original work, and that you have the right to grant the rights contained in this license. You also agree that your submission does not, to the best of your knowledge, infringe upon anyone's copyright.

If the submission contains material for which you do not hold copyright, you agree that you have obtained the unrestricted permission of the copyright owner to grant Dalhousie University the rights required by this license, and that such third-party owned material is clearly identified and acknowledged within the text or content of the submission.

If the submission is based upon work that has been sponsored or supported by an agency or organization other than Dalhousie University, you assert that you have fulfilled any right of review or other obligations required by such contract or agreement.

Dalhousie University will clearly identify your name(s) as the author(s) or owner(s) of the submission, and will not make any alteration to the content of the files that you have submitted.

If you have questions regarding this license please contact the repository manager at dalspace@dal.ca.

Grant the distribution license by signing and dating below.

_____   _____

Name of signatory   Date

ACKNOLEDGEMENTS

TABLE OF CONTENTS

LIST OF FIGURES

ABSTRACT

Mixed sand and gravel beaches are common along Canada's shoreline, however compared to their single sediment-type counterparts little work has been conducted. The purpose of this study is to contribute new understanding of mixed sand and gravel beach dynamics. More specifically, examine how waves affect the beach profile and the depth of sediment reworking during storms. Our study site, Black Rock Beach, is a planar steep examine how waves affect the beach profile and the depth of sediment reworking during storms. Our study site, Black Rock Beach, is a planar steep mixed sand and gravel beach with a 1:10 slope. The site is situated on the northern side of Minas Passage, on the Bay of Fundy. Understanding this interaction at our study site is important due to the potential for power generation in Minas Passage. Power will be brought to shore via cables buried in the beach, necessitating burial depths exceeding the maximum depth of disturbance.

An array of equally spaced depth of disturbance rods with free-sliding washers was deployed normal to the shoreline up the beach face. The array records the maximum depth of sediment disturbance and relative changes in bed elevation. Photos of the beach surface were taken along the rod array to examine surficial sediment composition change. Hydrostatic pressure and weather data were collected for the duration of the study, from 4 July to 5 September, 2014. Post-tropical storm Arthur was the only wave-generating event to have significant effects on the beach during our study. Significant wave heights up to 1.1 m, with winds up to 100 km1.1 m, with winds up to 100 km h^{-1} were generated during the storm. The maximum recorded depth of disturbance was 30.0 cm $\pm$ 0.4 cm near high-water, with decreasing depths seaward to about 7.1 cm $\pm$ 0.4 cm near low-water. A net increase in bed elevation was recorded, with values of 18.6 cm $\pm$ 0.4 cm about high-water and 1.1 cm $\pm$ 0.2 cm about low-water. Calmer beach conditions persisting through the rest of the study resulted in much shallower depths of disturbance, up to 5 cm, following a similar trend decreasing seaward. An updated method for estimating grain size from digital images using spatial autocorrelation was employed to examine surficial sediment compositions. Significant fining of the surficial sediment composition was recorded post-storm. Different forms of wave transformation, providing spatial and temporal controls on wave breaking, and the amount of energy dissipated through sediment reworking on Black Rock Beach are discussed.

Keywords: Bay of Fundy, Minas Passage, post-tropical storm Arthur, mixed sand and gravel, beach, depth of disturbance, wave transformation, spatial autocorrelation

LIST OF ABBREVIATIONS AND SYMBOLS

BoF: Bay of Fundy
BRB: Black Rock Beach
cm: Centimeter
c_p: Phase speed
D_{50}: Mass-median-diameter
DOD: Depth of disturbance
Eq: Equation
Fig: Figure
FORCE: Fundy Research Center for Energy
g: Gravitational acceleration
H: Deep-water wave height
h: Hour
h: Depth of water column
Ha: Measured bed elevation after wave wave action
HC: Hydraulic conductivity
Hd: Measured disturbed depth recorded after wave action
Hi: Measured bed elevation before wave action
Hs: Significant wave height
Hz: Hertz
k: Wavenumber
km: Kilometer
L_0: Deep-water wavelength
m: Meter
mm: Millimeter
MSG: Mixed sand and gravel
NNE: North-northeast
P-T: Pressure-temperature
PTS: Post-tropical storm
r: Spatial autocorrelation value
SAC: Spatial autocorrelation
tanh: Hyperbolic tangent
WSW: West-southwest
x_i: Intensity of a pixel in the reference plaquette
$\bar{x}$: Mean intensity of the reference plaquette
YD: 2014 year day
y_i: Intensity of a pixel in the offset plaquette
$\bar{y}$: Mean intensity of the offset plaquette
α: Angle of beach slope
$\Delta\eta$: Bed elevation change
ξ: Iribarren number
$\prod$: Phi scale of grain size
ω: Angular frequency

CHAPTER 1: INTRODUCTION

1.1 Opening Statement

     Little work has been conducted on mixed sand and gravel (MSG) beaches compared to their single sediment type counterparts. They compose a significant proportion of Canada's shoreline despite being comparatively rare on a global scale. Black Rock Beach (BRB) is a MSG beach located on the northern side of the Minas Passage, about 7 km southwest of Parrsboro, on the Bay of Fundy (BoF) (Fig. 1.1). It is also the location of the Fundy Ocean Research Centre for Energy (FORCE) test site for in-stream tidal energy technology. The high flow velocities in the passage corresponding to the high tidal ranges in the region make the site ideal for tidal energy research. Understanding the interaction between the beach and incoming waves is particularly important at this site due to its potential for power generation just offshore. Waves generated locally from storms arrive at the beach dispersing and reflecting stored energy. Much of the energy is dissipated through wave breaking, reworking beach sediments, creating an active layer; the depth of this reworking is referred to as depth of disturbance (DOD). The purposes of this study are: (1) to contribute to our understanding of how MSG beaches operate, (2) to examine how waves affect the beach profile and DOD, and (3) to recommend a minimum depth for cable burial.
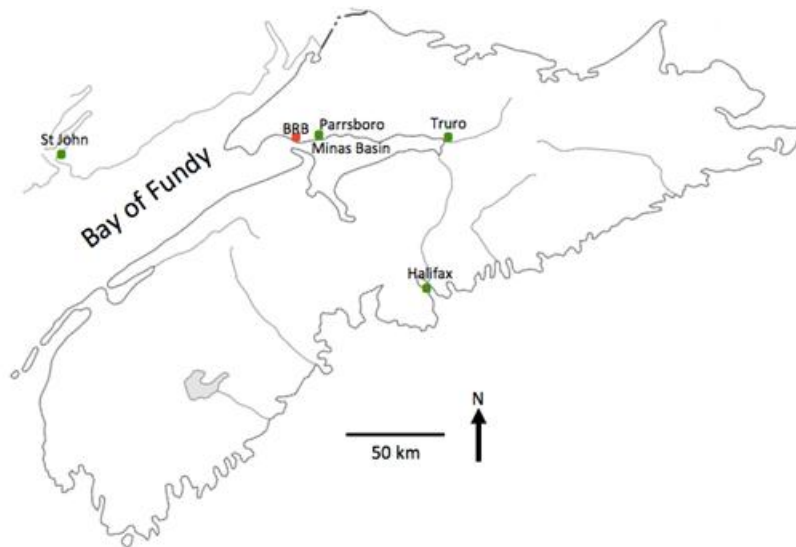
Figure 1.1 Map of southern Nova Scotia identifying BRB indicated in red. (Modified from http://atlas.gc.ca)

1.2 Geologic Setting and History

The geology of the Canadian Maritimes can be divided into two general regions, the Atlantic Uplands and the Carboniferous-Triassic Lowlands. The BoF lies in the domain of the Carboniferous lowlands, and is underlain by Triassic sandstones, shales, and basalts (Parrott et al. 2008). Geologically the study site is positioned near the contact between the North Mountain Formation, composed of tholeiitic basalt, and the Boss Point Formation, composed of alluvial conglomerate and sandstone (Keppie, 2000). The North Mountain basalts, Jurassic in age, also compose much of the southern BoF shoreline across the passage.

The formation of the Fundy basin began in the middle Triassic due to rifting of the region associated with structural weaknesses formed from Paleozoic compressional structures related to the Appalachian orogeny. Withjack et al. (1995) describe the formation of the Fundy rift basin in three distinct phases, instead of solely by rifting and drifting as in most tectonic models. From the middle Triassic to early Jurassic, synsedimentary extension occurred along reactivated Paleozoic compressional structures. Displacement exceeded 10 km along the associated faulting, sedimentation

and extrusive volcanic deposits of up to 3 km in some parts took place over this period of basin formation. A phase of shortening followed rifting in response to compression in the region. As a result, there was reverse faulting and compressional deformation resulting synclinal forms in sub-basins of the bay. Early drifting and eventually abandonment of the rift followed.

1.3 Oceanologic Setting

BRB lies on the shore of Minas Passage in the BoF. The BoF is known for the highest reported tides in the world, with tides ranging from about 4 m at the mouth of the bay and increasing to as high at 17 m in the head of the bay (O'Reilly et al., 2005). This large tidal range is due to a resonant period in the bay of about 13 hours, closely matching the lunar tidal cycle of about 12 hours and 25 minutes. Minas Passage, about 5 km wide, is a strait connecting the Minas Basin to the rest of the bay. This confined geography and large tidal range result in swift current velocities in Minas Passage. The sheltered geography also controls wave climate, preventing large swells originating in the open ocean from reaching inner parts of the bay. Waves are generally limited to locally generated wind waves. Ideal wave generating conditions in the BoF would have strong, persistent winds blowing from the WSW up the full length of the bay (Fig. 1.1).

Detailed bathymetric studies in the region, shown in Figure 1.2, conducted by the Geological Survey of Canada and the Canadian Hydrographic Service in 2006 revealed an erosional scour trench in the Minas Passage, about 170 m deep, due to high current velocities (Parrott et al., 2008).
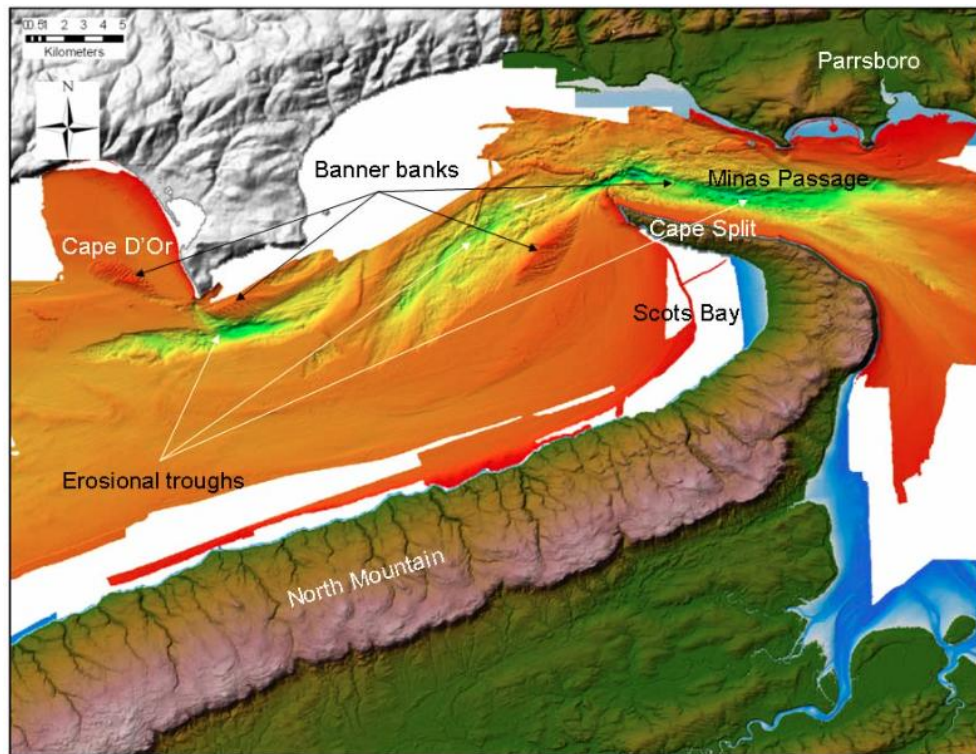
Figure 1.2 The BoF seafloor partially mapped using multibeam bathymetric mapping from Cape D'Or to the Minas Passage (Parrott et al., 2008)

1.4 Beach Morphology and Composition

BRB is a steep, planar, MSG beach with a slope of about 1:10, extending about 120 m from low tide landward (Fig. 1.3). The beach grades to a salt marsh landward and is bound by basalt cliffs, forming a small headland to the east. The active profile of the beach, between high and low tides, is planar and makes up the lower 90 m of the beach face. The upper 10 m is composed of the storm berm that grades into a salt marsh. Directly offshore, below lowest low tide, the slope becomes much shallower: about 1:30.
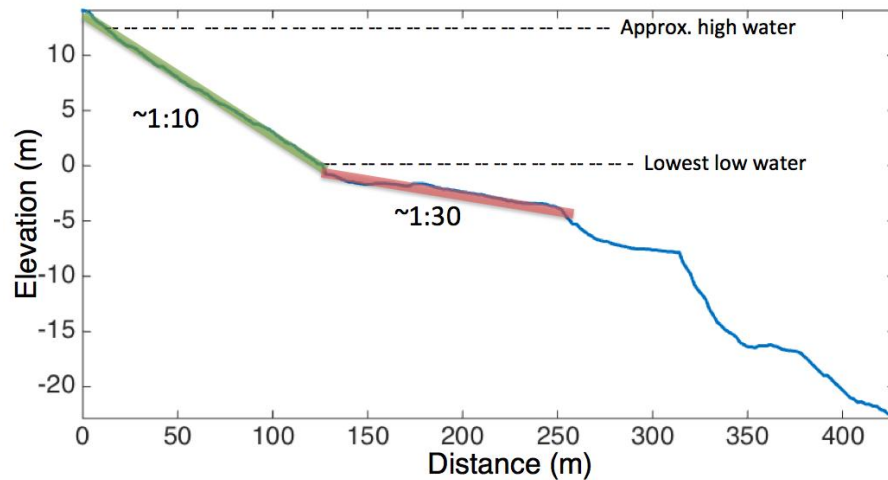
Figure 1.3 Absolute beach elevation and offshore bathymetry of BRB using lowest low water as reference. The active beach slope, about 1:10, is highlighted in green. The immediate offshore slope, about 1:30, is highlighted in red; data provided by FORCE.

The beach is composed of unconsolidated sediment varying from boulder to sand in size. The grains are generally well rounded and flat, with the exception of angular to sub-angular basalt grains, which have recently been eroded from the adjacent cliffs. The geology of the region is reflected in the lithological composition of the beach, composed mostly of sediments from the Boss Point Formation with grey to greenish-grey quatzose sandstones, minor red fine grained sandstones, and minor grey shales. Volcanic clasts of basalt, originating from the North Mountain Formation, also compose a small portion of the beach.

1.5 Beach Processes and Hydrodynamics

Depth of disturbance is directly related to wave breaking, swash hydrodynamics, hydraulic conductivity and the grain size distribution of the beach face sediments. Wave breaking is the most important factor affecting depth of disturbance because there is direct transfer of energy from waves to the beach face. There are many processes that govern sediment motion on mixed sand and gravel beaches, as outlined by Mason & Coates (2001). Hydraulic conductivity, infiltration and groundwater,

wave reflection, and threshold motion are first order factors. Tidal range, specific gravity, clast shape, and chemical processes are second order factors.

Hydraulic conductivity (HC) describes the ability for fluid to pass through pore spaces. On beaches the process is important in determining the direction of sediment transport and beach slope. Quick & Dyksterhuis (1994) suggest that more conductive beaches produce a net onshore shear stress from the swash and backwash cycles of breaking waves. Few field measurements of HC have been made on MSG beaches. However laboratory measurements have shown that the sand fraction is the most important factor in HC (Mason & Coates, 2001). A sand fraction of about 25%, indicated from multiple studies (Mason & Coates, 2001), is a key value in determining the HC. Less than ~25% sand yields higher values of HC more similar to pure gravel and at about 25% and greater the response is more similar to sand, with HC reduced up to two orders of magnitude. Infiltration seepage and groundwater, dependent on HC, is also important in determining sediment motion because it determines the amount of energy dissipated during infiltration of swash and backwash and saturation of the sediments. The groundwater response of MSG beaches is similar to sand with lower HC and increased water retention.

Wave reflection is the return of wave energy offshore that has not been absorbed or transferred to the beach surface. Reflection coefficients can vary from 0.1 to 0.6 depending on the beach and wave characteristics (Powell, 1988; Mason, 1997). Wave steepness, beach slope, grain size, friction on the sediment-water interface, and infiltration capacity are all factors affecting the amount of wave energy reflected from a beach. Grain size is the most important factor in determining the wave reflection because it is related to bed roughness, infiltration capacity, permeability, and beach slope. Coarse gravel beaches are able to absorb more energy than sand beaches of similar slope due to increased bed roughness, infiltration capacity, and hydraulic conductivity, resulting in decreased reflected wave energy. In MSG beaches the contribution of sand decreases the ability for energy to be attenuated

through infiltration, although slopes are steeper than sand beaches resulting in greater proportions of wave reflection.

The threshold of motion is the critical fluid velocity above which individual grains are mobilized and is important for conditions, which produce shear stresses near the threshold. It is difficult to quantify for mixed beaches because of the great variability of grain size. The threshold of motion is assumed to be substantially surpassed during the significant wave events for our study.

Tidal range is the most important secondary factor to consider at BRB since tides can exceed 13 m. In previous studies the importance of tidal range is noted due to the variability in beach slope with the changing tides, affecting the position of wave breaking and wave breaking type, and thus affecting DOD (King, 1951; Beach & Stenberg, 1996). It is also important to consider BRB is limited to locally generated wind waves rather than lower frequency swells generated far offshore. Powell (1988) reported that these steeper, locally generated waves are more efficient at dissipating wave energy due to wave breaking and frictional loss.

1.6 Previous Studies

The first DOD study was conducted by King (1951) on a sandy beach and many have followed since. Average DOD and wave heights on sand beaches, compiled from previous studies by Anfuso (2005), ranged from 1.8 cm to 22 cm and from 34 cm to 111 cm for wave heights. Anfuso (2005), using the compiled data, determined that beach slope and breaking wave height are the most important factors in DOD because they control breaking wave type. Linear regressions relating the parameters beach slope, breaking wave height, and disturbance depth have been made for sand beaches (Anfuso, 2005; Ciavola et al., 1997). However none have been made for MSG beaches.

Ivamy and Kench (2006) conducted one of the few studies of DOD on MSG beaches. The study found DOD was highest near the break-point step, an along shore bar about low-tide, exceeding 540

mm, and decreased landward to 1 mm. Break-point step migration was also observed, the step migrated landward with the rising tide and returned to its initial position at low tide. The study showed the break-point step controlled DOD because it acts as a filter, causing steeper short period waves to break at the step and allowing longer period swell waves to propagate to higher sections of the beach. The tides also provided temporal controls on wave filtering at the break-point step, allowing all wave energy to propagate on to the lower beach face at about mean water levels up to 2/3 of high tide.

Saini et al. (2009) also examined DOD on MSG on a beach in Delaware Bay. Significant wave height ranged from 0.18 to 0.40, with DOD from 0.02 to 0.12 cm.

CHAPTER 2: METHODOLOGY

2.1 Depth of Disturbance Rods

The use of DOD rods, originally developed by Greenwood and Hale (1980), is the primary method used for this study. Greenwood and Hale (1980) showed that the rods record no significant difference between DOD estimates from other standard methods, such as tracers. Thus, our study uses an array of equally spaced rods, 1.3 cm in diameter and 1.8 m in length with free-sliding washers, deployed normal to the shoreline up the beach face (Fig. 2.1). The rod array followed about a 70 m traverse and the rods were spaced 17 m ($\pm$ 20 cm) apart. Hammers were used to drive the rods into the beach face to a depth of about 1.3 m, leaving 30 cm to 50 cm exposed above the beach surface.
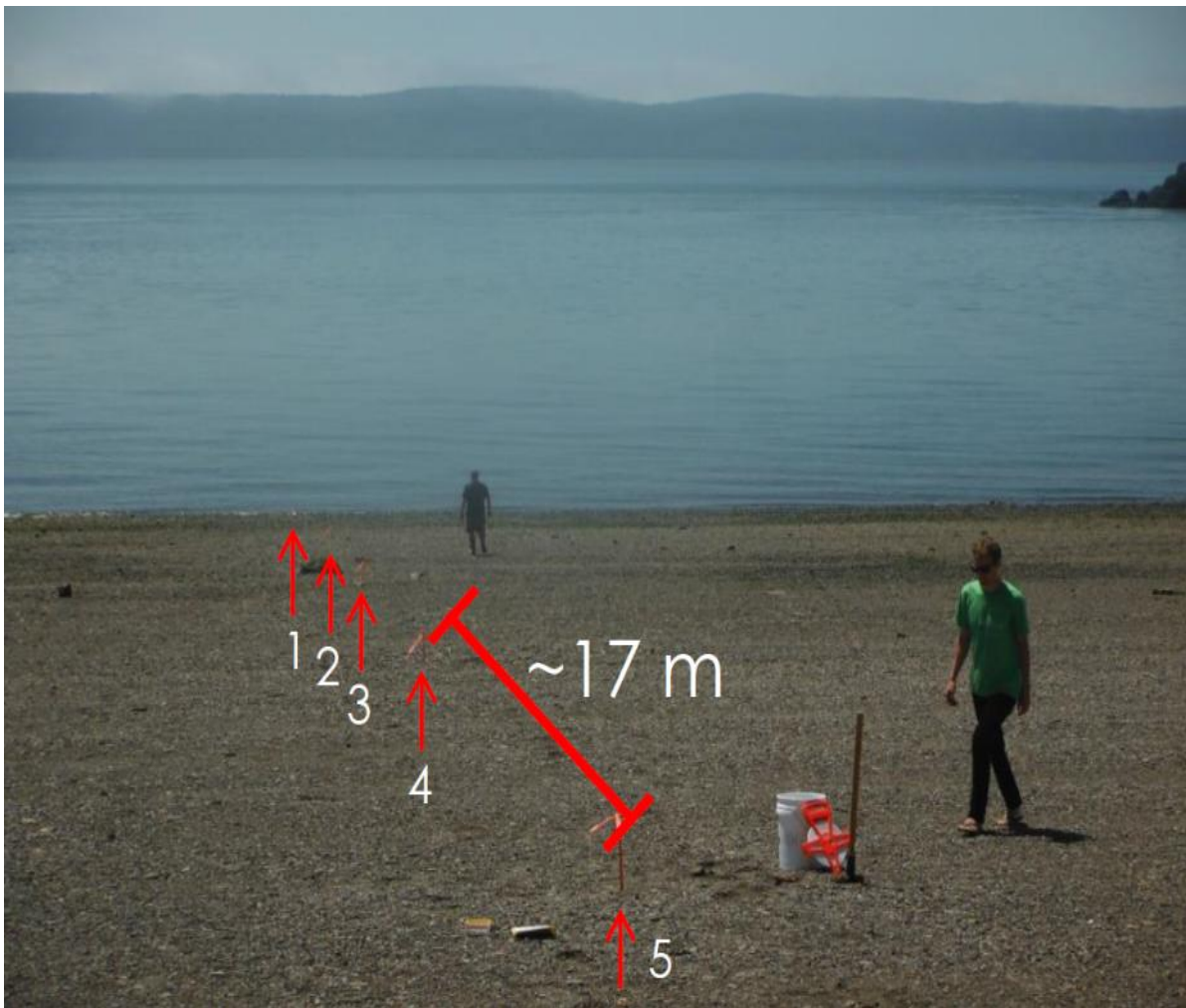
Figure 2.1 The DOD rod array setup for this study, numbered 1 to 5 from low to high on the beach face.

The washers record the initial, disturbed, and aggraded depths relative to the top of the rod shown in Figure 2.2. The initial beach surface is used as a reference point for degradation and aggradation; measured relative to the top of the rod (Hi) before a wave event. During wave action subsequent degradation occurs, which suspends the beach sediments allowing the free-sliding washers to fall. As wave action diminishes sediment is accreted over the washer burying it. After the wave event the reworked beach surface recorded (Ha) and the washer depth (Hd) are recorded, and the washer is placed back on the beach face. DOD and bed elevation change, $\Delta\eta$, was determined as follows

$$DOD = Hi - Hd \tag{2.1}$$

$$\Delta\eta = Hi - Ha \tag{2.2}$$

where the different H's are defined in Figure 2.2. With these definitions, DOD should always be less than or equal to 0, while $\Delta\eta$ may be positive (accretion) or negative (erosion).
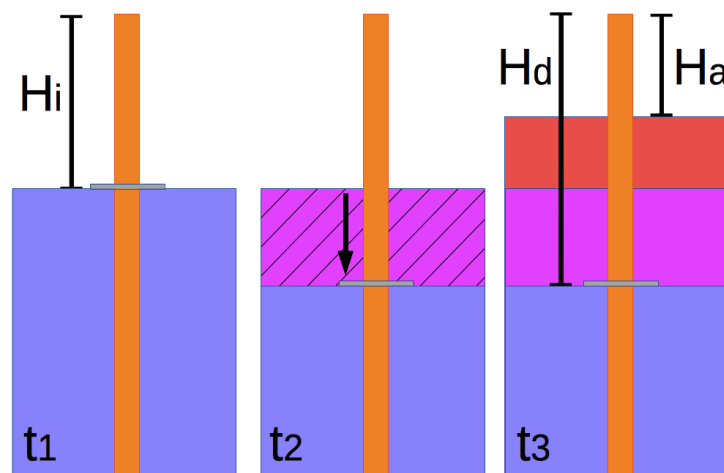
Figure 2.2 The process in which accreted and disturbed depths are recorded using DOD rods. At time t1 a free-sliding washer is placed through the rod at the surface of the beach. With subsequent wave action at time t2 sediment is entrained allowing the washer to fall, recording the DOD, marked in pink. As wave action subsides accretion (positive $\Delta\eta$) or erosion (negative $\Delta\eta$) –accretion in the case of this figure -- may occur relative to the initial washer position, marked in red at time t3.

2.2 Pressure-Temperature Sensors and Wind Data

Two RBRduo P-T sensors were used to collect pressure data, one installed by FORCE and the other by the Dalhousie Department of Oceanography. The FORCE sensor, under about 10 m of water at high tide, was initially intended by FORCE for use as a tide gauge. It was modified for this study to sample more frequently, at four hertz, for a better wave signal. The Dalhousie gauge, also sampling at four hertz, was installed at about mid-beach (Fig. 2.3), buried about 50 cm depth, along the rod array. The pressure sensors operate using strain gauge sensors, which generate different levels of voltage in response to changes in pressure. Pressure sensors can be used to determine wave motion because passing waves cause the pressure to change through the water column, called the perturbation pressure. The perturbation pressure decays with depth in the water column, making changes of wave height harder to detect at greater depths. The temperature data collected from the gauges were not used for this study.

Figure 2.3 Installation of the Dalhousie pressure sensor near mid-beach at about 50 cm depth.

Wind data are collected because it can be used to understand changes in wave conditions. A weather station at the FORCE visitor centre 200 m NNE of the study site provided wind speed and direction data.

2.3 Photo Survey and Sieve Analysis

A photo survey of the beach surface was conducted during each visit to the site to determine the grain size distribution of the surficial sediments. The survey followed a traverse along the DOD rod array. A camera was attached to a mount to ensure the distance from the camera to the beach surface stayed constant (Fig. 2.4). The photos are spaced about 10 m apart, with 11 photos of the beach surface taken along the traverse. The photos from the survey are processed using a method developed by Rubin (2004), described in the data processing section.
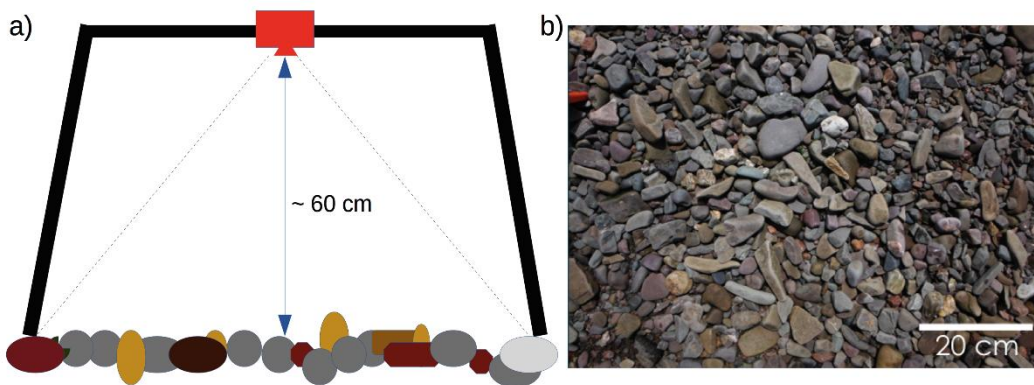
Figure 2.4 a) Camera and mount during the photo survey, b) a sample image of the beach surface.

Sieve analysis was conducted on two core samples and a surficial sediment sample to determine the general sediment-size composition of the beach. The surficial sediment sample was taken at about mid-beach, covering an area of approximately 1 m x 1 m and about 7 cm depth. The core samples were taken at about mid-beach and at upper-beach, at about 13 cm depth and 25 cm depth. Sieves ranging from 64 mm to 1/16 mm were used. After determining general sediment distribution the sieved sediments were used to as calibration sizes for the autocorrelation method described in the data processing section.

2.4 Data Processing

2.4.1 Wave Statistics

The pressure sensors record changes in pressure for the duration of their deployment. Processing the pressure data is important to isolate wave data, which can later be related to sediment reworking. Low-frequency waves, such as tides, are first removed using a high-pass digital filter (Fig. 2.5), allowing higher frequency waves generated during storm events to be examined.
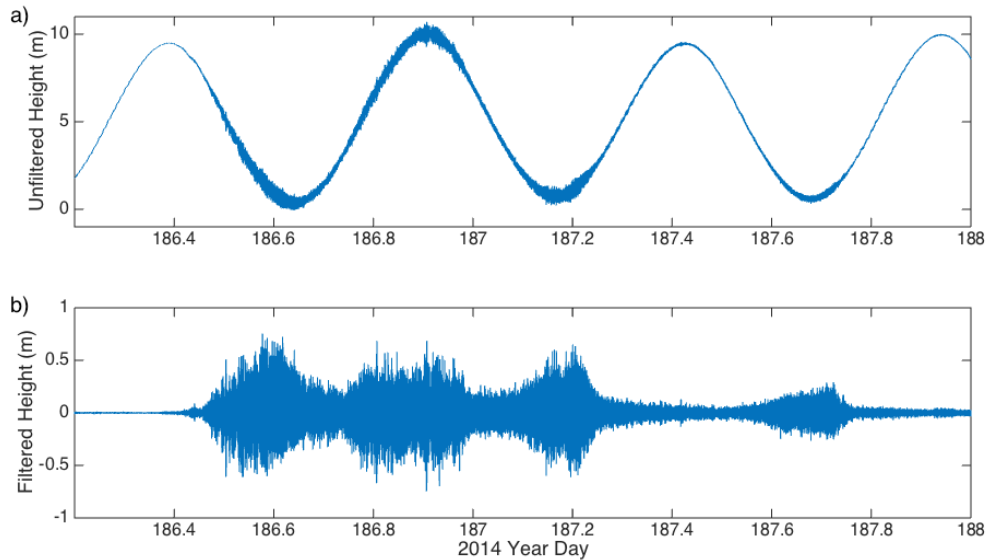
Figure 2.5 a) The unprocessed wave data and b) filtered wave data removing of low frequency pressure variations related to the tides.

After the lower frequency signals have been removed further processing of the data can be done. Using the dispersion relation (Eq. 2.3), simplified for deep-water waves (Eq. 2.4) and spectral analysis, values of significant wave heights and wave periods were obtained. The dispersion relation (Eq. 2.3) and the dispersion relation simplified for deep-water waves (Eq. 2.4) are given as follows

$$\omega^2 = gk\tanh{(kh)} \tag{2.3}$$

$$\omega^2 = gk \tag{2.4}$$

where ω is angular frequency, g is gravitational acceleration, k is wavenumber, and h is depth of the water column.

2.4.2 Spatial Autocorrelation of Beach Sediments

The photos collected from the photo survey are processed using a method developed by Rubin (2004) where autocorrelation between pixels in images of sediment are used to determine the grain size distribution. Spatial autocorrelation (SAC), defined by Rubin (2004), is the correlation of the intensity (brightness) between two rectangular regions of equal size, referred to as plaquettes, in an image. First the image is converted to grayscale so that intensity values of the images can be assigned. The first plaquette is the reference region, and the second plaquette is displaced by a certain number of pixels from reference region, referred to as pixel offset, across the original image (Fig. 2.6). The intensity of a pixel in the reference plaquette is correlated with the corresponding pixel in the displaced plaquette. Calculating the correlation for each pixel in the rectangles gives the SAC value, r (Eq. 2.3), for the plaquettes for that pixel offset. The correlation calculation is repeated for each pixel offset, up to an offset of 200 pixels, allowing a curve to be generated with SAC against pixel offset.
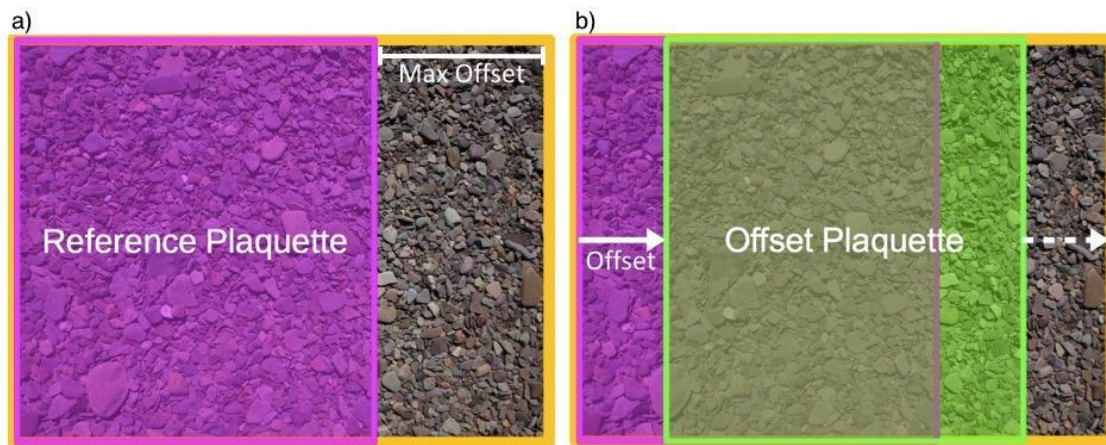
Figure 2.6 a) The reference plaquette used for spatial autocorrelation with maximum offset marked, b) the offset plaquette shifted by a pixel offset.

$$r = \frac{\sum_i (x_i - \bar{x})(y_i - \bar{y})}{\sqrt{\sum_i (x_i - \bar{x})^2}\sqrt{\sum_i (y_i - \bar{y})^2}}$$

(2.3)

where r is the SAC value, x_i refers to the intensity of a pixel in the reference plaquette, y_i refers to intensity of a pixel in the offset plaquette, $\bar{x}$ refers to the mean intensity of the reference plaquette, and $\bar{y}$ is the mean intensity of the offset plaquette.

A smaller pixel offset results in SAC values closer to 1 because pixels in the displaced plaquette will have similar intensity values as the reference plaquette. As pixel offset becomes larger relative to grain size the values approach 0. Curves are generated from photos of reference size-fractions and photos of mixed size-fractions so sediment distributions of the mixed image can be estimated using this method. An example of generated curves are shown in Figure 2.7a.

The sediment size distribution is determined by comparing the generated curve of a sediment sample to the curves of the calibrated samples and solving for proportions of calibrated sizes that give the best fit for the curve of the sample. The best-fit curve is determined using a special case of the least-squares fit method, non-negative least squares, to determine size distributions. Rubin's original method was modified for our study in several ways. First, a cut-off value of 0.05 was chosen because the curves typically did not show any useful information below this value (Fig. 2.7a). Second, a method using the cumulative sum of the SAC (Fig. 2.7b) was developed to prevent curves from intersecting and to better estimate the sand fraction. Lastly, instead of calculating the SAC values for a whole image, the image was segmented into 12 equally sized regions where SAC calculations were done individually, and size fraction estimates were averaged from the 12 segments for the entire image. This gave better local approximations of sediment size proportions within an image and allowed an error estimate to be determined in each size interval: i.e. the standard deviation of the 12 estimates.
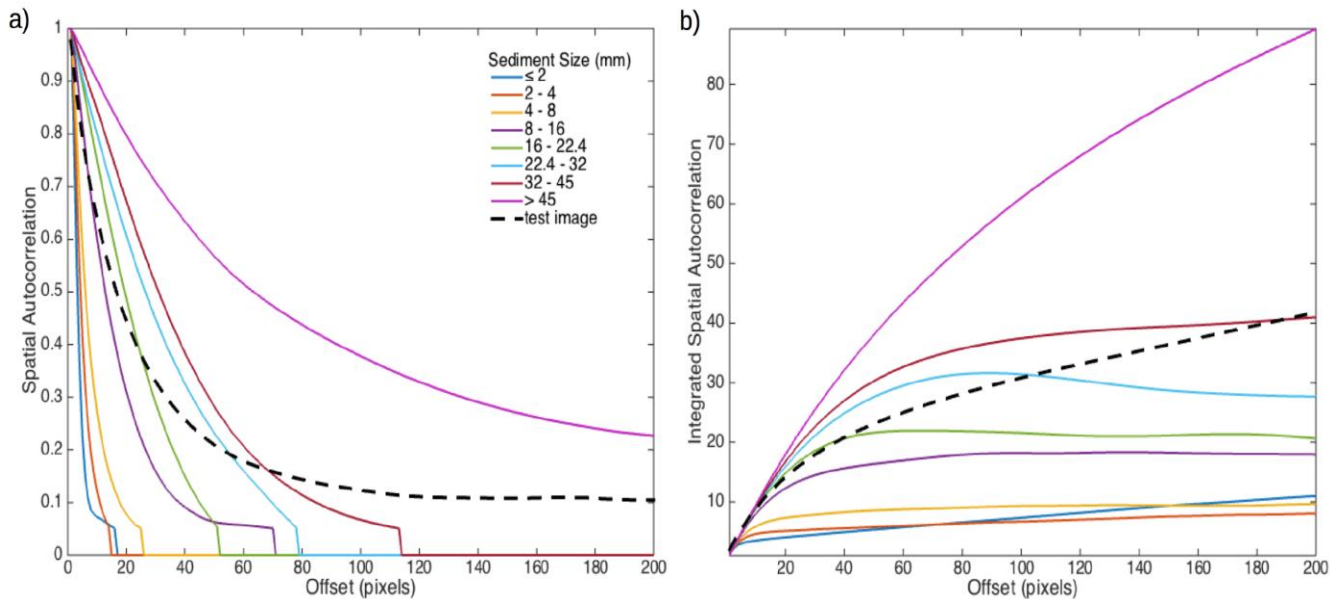
Figure 2.7 Spatial autocorrelation against pixel offset for calibrated sizes, and a test sample; a) using Rubin's method b) cumulative sum method.

An example of this method applied to coarse beach material is shown in Figure 2.8 and to finer material in Figure 2.9. From Figure 2.8a coarse sediment with diameters greater than 2 cm make up the majority of the image, with some finer material in the spaces between the larger grains. Both the Rubin method (Fig. 2.8b) and the cumulative sum method (Fig. 2.8c) provide reasonable estimates of surficial beach composition, showing the majority of the surface is coarser than 2 cm, however the finer portions seem to be underestimated. Figure 2.9a shows a sample with finer material, generally less than 3 cm in diameter with sand composing a significant portion. The cumulative sum method of estimation (Fig. 2.9c) showed better results than the Rubin method (Fig. 2.9b), estimating about 22% sand by surface area, whereas the Rubin method estimated the sand portion to be nearly zero. Error values are large due to variations in size estimation for different segments of the image.

Figure 2.8 Size estimations for an image of coarse beach sediments (a) using the Rubin method (b) and the cumulative sum method (c) with blue lines indicating the estimated value and dashed yellow indicating error using the standard deviation of the 12 images

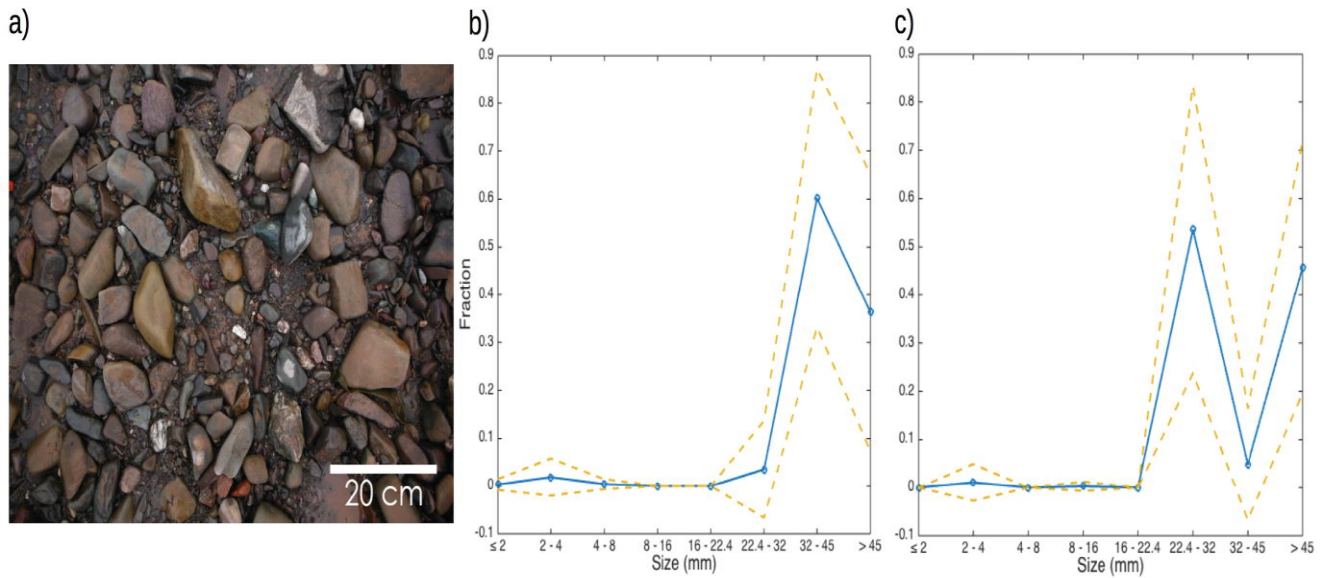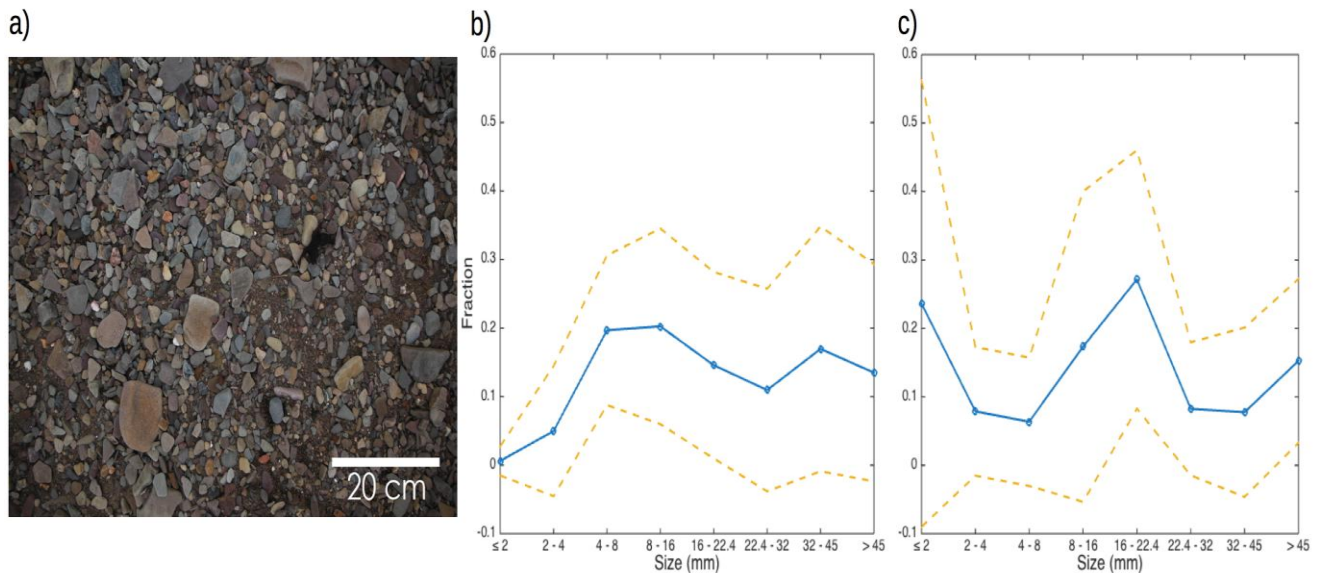Figure 2.9 Size estimations for an image of finer beach sediments (a) using the Rubin method (b) and the cumulative sum method (c) with blue lines indicating the estimated value and dashed yellow indicating error using the standard deviation of the 12 images

CHAPTER 3: RESULTS

3.1 Beach Composition

A bulk sample, 1 m x 1 m area and 7 cm deep, of surficial sediments, taken from mid-beach level on 20 June 2014, was sieved to determine the general sediment-size composition of the beach. The sieve analysis showed the distribution to be predominantly bimodal (Fig. 3.1) with 72% gravel sized and coarser (> 2 mm) and 28% sand sized and finer (< 2 mm). The mass-median-diameter (D_{50}) was interpolated to be about -4.0 $\prod$ or 16.0 mm. The fraction of silt and clay comprises less than 1 percent of total mass and its role in beach processes is assumed to be insignificant, and is neglected in the study.
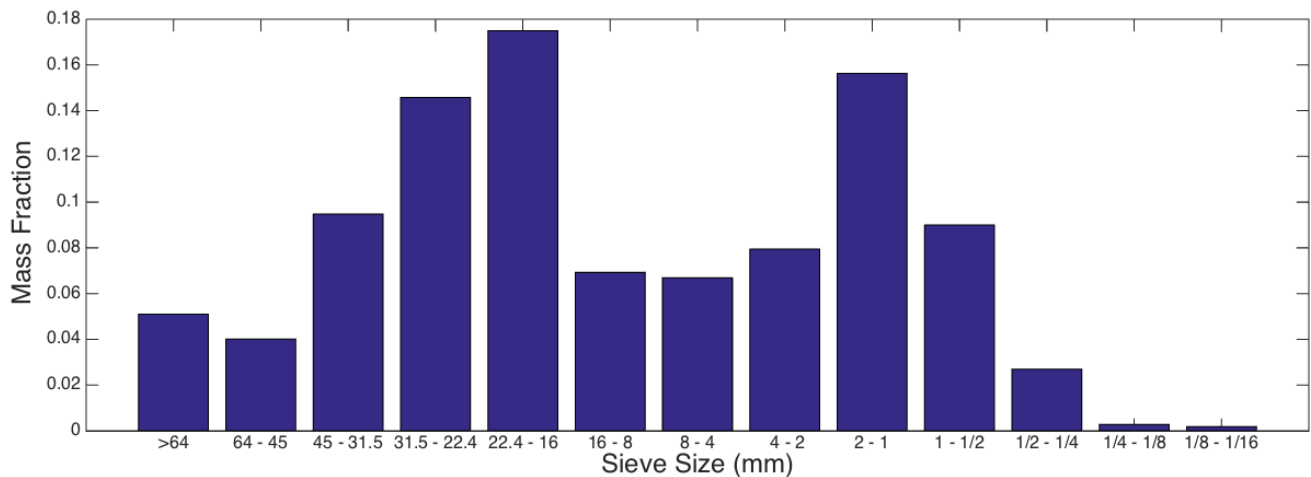
Figure 3.1 Sediment size distribution of the bulk surficial sediment sample, exhibiting the modal distribution on either side of the 4-8 mm size fraction, with mean diameters of 1-2 mm for the finer fraction, and about 20 to 25 mm for the coarser.

Core samples of the beach surface were taken on 1 August 2014 to examine size distribution with depth. Core 1 (Fig. 3.2a) was taken at about the mid-tide line to 12.6 cm depth, and core 2 (Fig. 3.2b) was taken near the high-tide line to 24.6 cm depth. The core samples also exhibit a bimodal distribution similar to the surficial sample, although the bimodality is not as prominent in core 2 and seems to level off with depth.
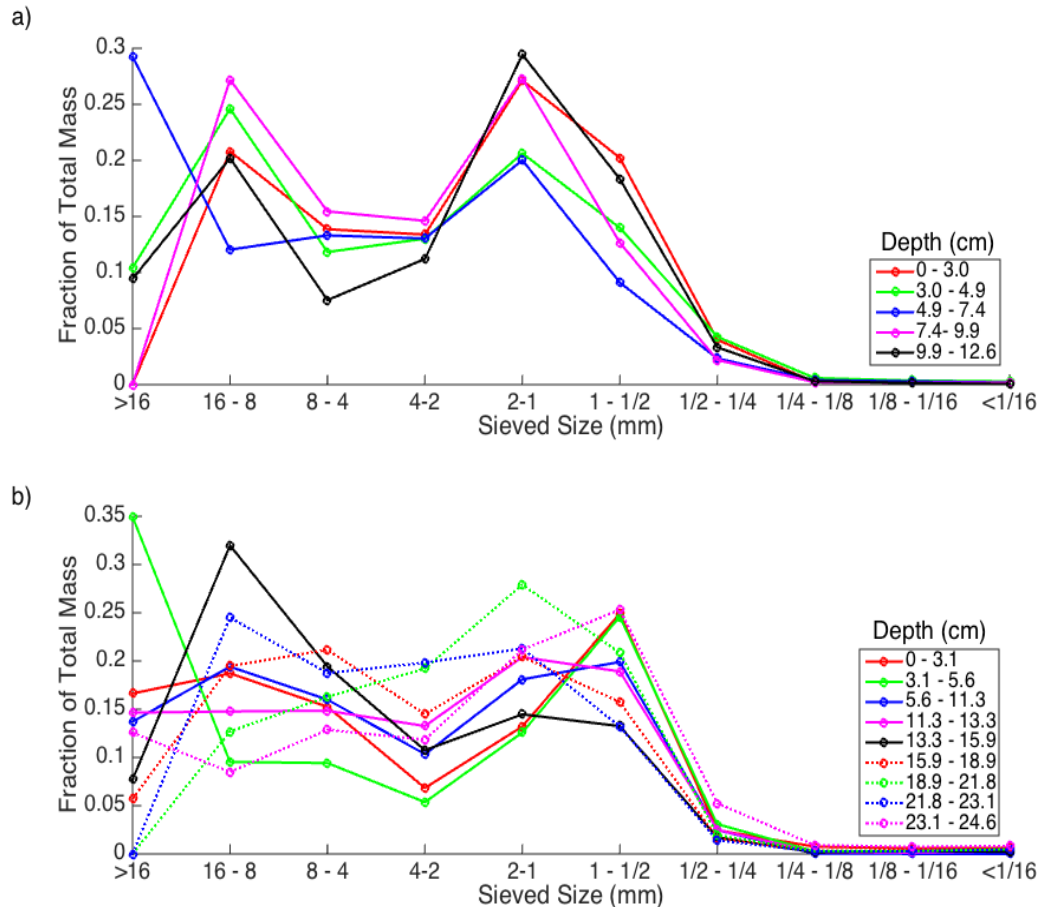
Figure 3.2 Sediment size distribution of core samples a) core 1 taken at about mid-beach b) core 2 taken near the high tide line.

3.2 Overall Forcing Conditions

Time series of significant wave height (Hs), tidal elevation, and wind speed during the course of the 2-month study are shown in Figure 3.3. The study was conducted from 4 July (YD 185) to 5 September (YD 248). The data in figure 4.3 end on 24 August (YD 236) and a gap in data is present on 23 July (YD 204). The only significant wave event was post-tropical storm (PTS) Arthur on 5 and 6 July (YD 186-187). Waves recorded for the remainder of the study exhibit significant wave height less than 20 cm. Neap tide range was observed to be 9.2 m. Due to the position of the FORCE tide gauge being just above low water during spring tides, ranges were not completely recorded, however, using interpolation, the largest spring tide was estimated to be about 13.5 m.
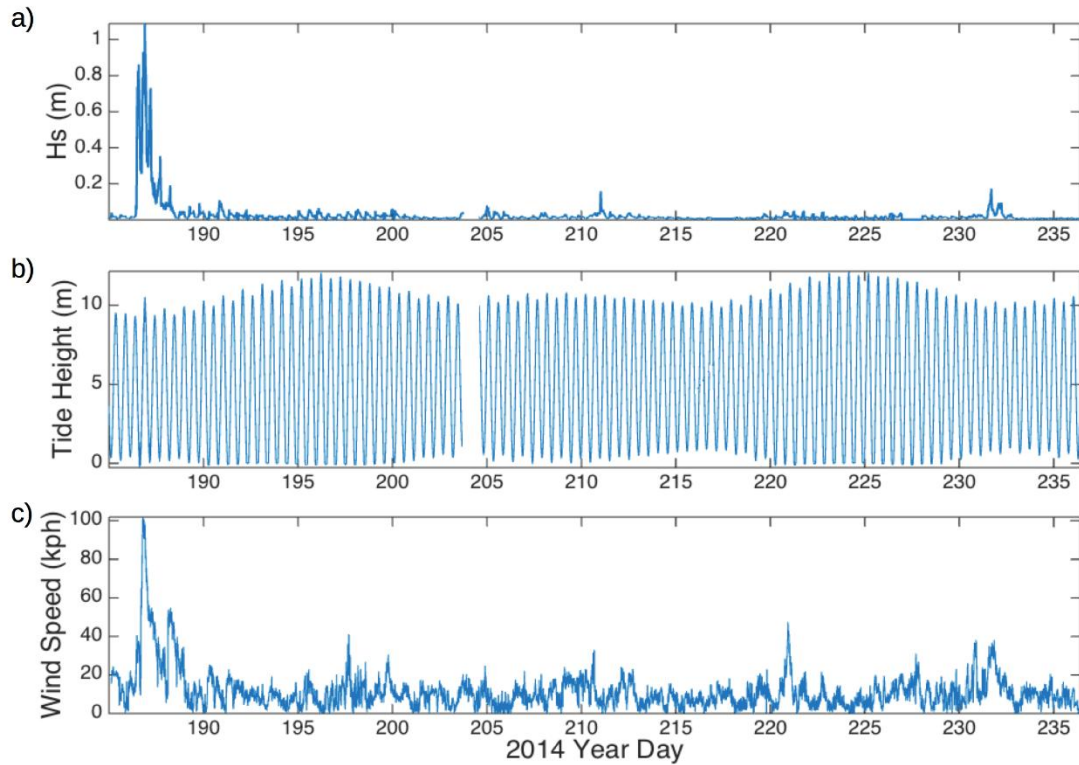
Figure 3.3 Time series from 4 July to 24 August 2014, a) significant wave height (*Hs*), b) tide height, and c) wind speed.

3.3 Calm Conditions

Non-storm conditions made up the vast majority of the study period, from 7 July to 5 September, resulting in much shallower DOD.

3.3.1 Wave Conditions

The sheltered geography of the Bay of Fundy and or study site prevents large swell waves, generated by distant storms, from reaching BRB. Thus, large waves are typically limited to local storm events passing through the region. Calm conditions, spanning most of the study period, typically did not exceed 20 cm in wave height and did not last more than a few hours. Winds (Fig. 3.3c) typically ranged from 2 - 20 km h^{-1}, with only three events, producing winds as high as 40 km h^{-1}. However, these events did not persist long enough to produce large waves. A sample of the wave conditions from

17 July to 22 July of both Force and Dalhousie gauges are shown in Figure 3.4. A maximum wave

height of about 7 cm was observed for this period, with the Dalhousie gauge recording higher waves

due to steepening as the waves approach shore. Wave transformation is also visible, best seen in Figure

3.4a, where abrupt decrease in wave height occurs during ebb tide. At the FORCE gauge (Fig. 3.4a),

wave heights are generally highest just after low tide and generally decrease as the water level

increases. The Dalhousie gauge, installed at mid-beach, often show maxima in wave heights as the tide

recedes and approaches about the gauge, making a contorted V or U-shape trend in wave heights as the

tides oscillate above the gauge.
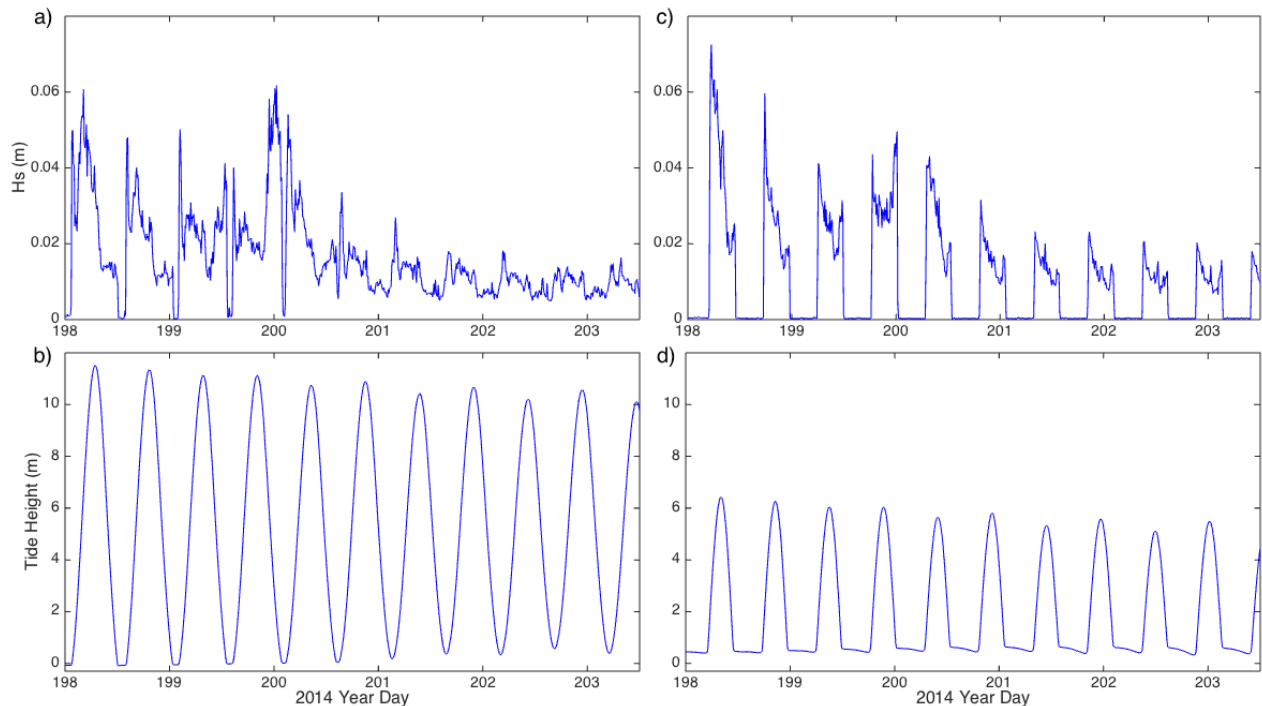
Figure 3.4 Significant wave height and tide height from July 17th (YD 198) to 22th (YD 204) a) and b) data collected at the FORCE gauge, installed about low tide c) and d) data collected from the Dalhousie gauge, installed about mid-beach

3.3.2 Depth of Disturbance

The DOD rods recorded a general trend of increasing DOD landward throughout the study. The

calm beach conditions produced shallow depths of disturbance ranging from virtually no change near

low tide at rods 1 and 2 up to a maximum of 4.9 cm near high tide at rod 5 over the duration of the

study. An example of DOD values during calm conditions is shown Figure 3.5 based on data collected from 8 and 16 July. The most seaward rods, 1, 2 and 3, show the least reworking, with DOD values of about 2 cm and higher values landward at rods 4 and 5. The $\Delta\eta$ values exhibit both accretion (positive) and erosion (negative). Tables for the depth of disturbance rods are provided in Appendix A.
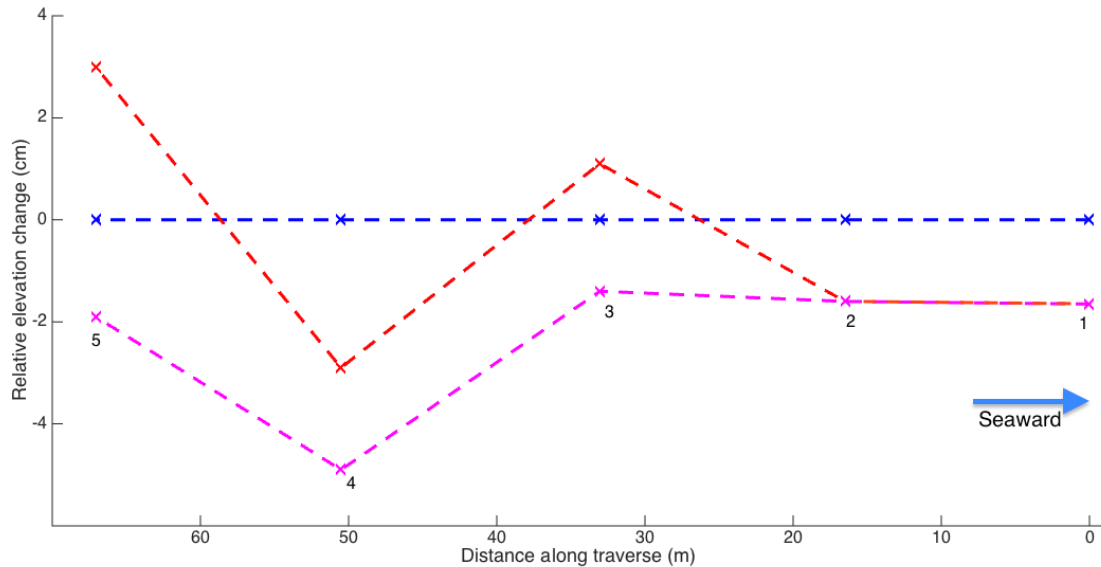
Figure 3.5 DOD values (pink) and bed elevation change, $\Delta\eta$ (red) on 16 July, relative to the 8 July surface used as reference (blue)

3.4 Post-Tropical Storm Arthur

Arthur made landfall during our study on 5 July (YD 186), and was responsible for the only major wave event during this study. The storm developed into a category 2 hurricane off the southeastern coast of the United States and progressively lost energy as it made its way north, being reclassified as a post-tropical storm before making landfall over Atlantic Canada. The storm tracked through the Fundy Basin creating ideal conditions for wave generation in the bay.

3.4.1 Wave Conditions

Arthur generated winds of up to 100 km h^{-1} (Fig. 3.6), predominantly from the west, resulting in significant wave heights of up to 1.1 m and wave periods from 4 to 8 s (Fig. 3.7). Wave data, shown in Figure 3.7a, show three distinct periods of higher waves, a result of complex wave modulation. The first waves arrived about seven hours before peak wind conditions. Timing of the waves and tidal stage are important to note, where the highest waves (Hs ~1.1), correspond with the high tide and peak wind conditions. Winds of up to 40 km h^{-1} persisted until about 7 July (YD 188). Wave heights gradually returned to values typical of calm conditions as the wind subsided to less than 20 km h^{-1} on 6 July (YD187).
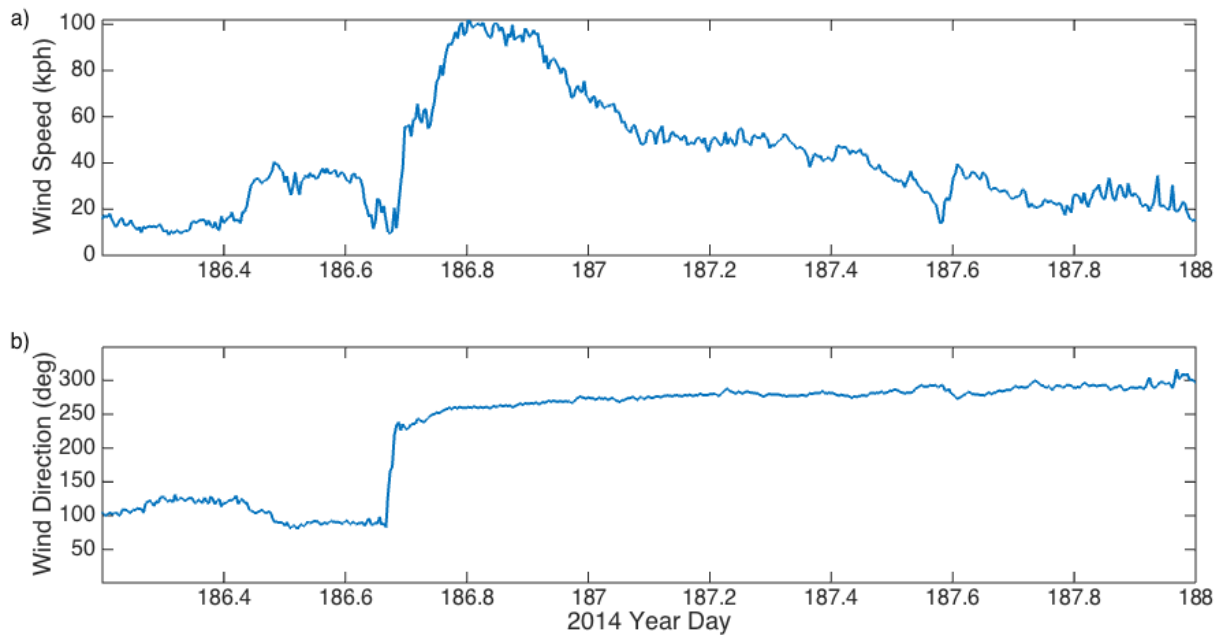
Figure 3.6 Wind conditions during PTSA; a) wind speeds and b) wind direction
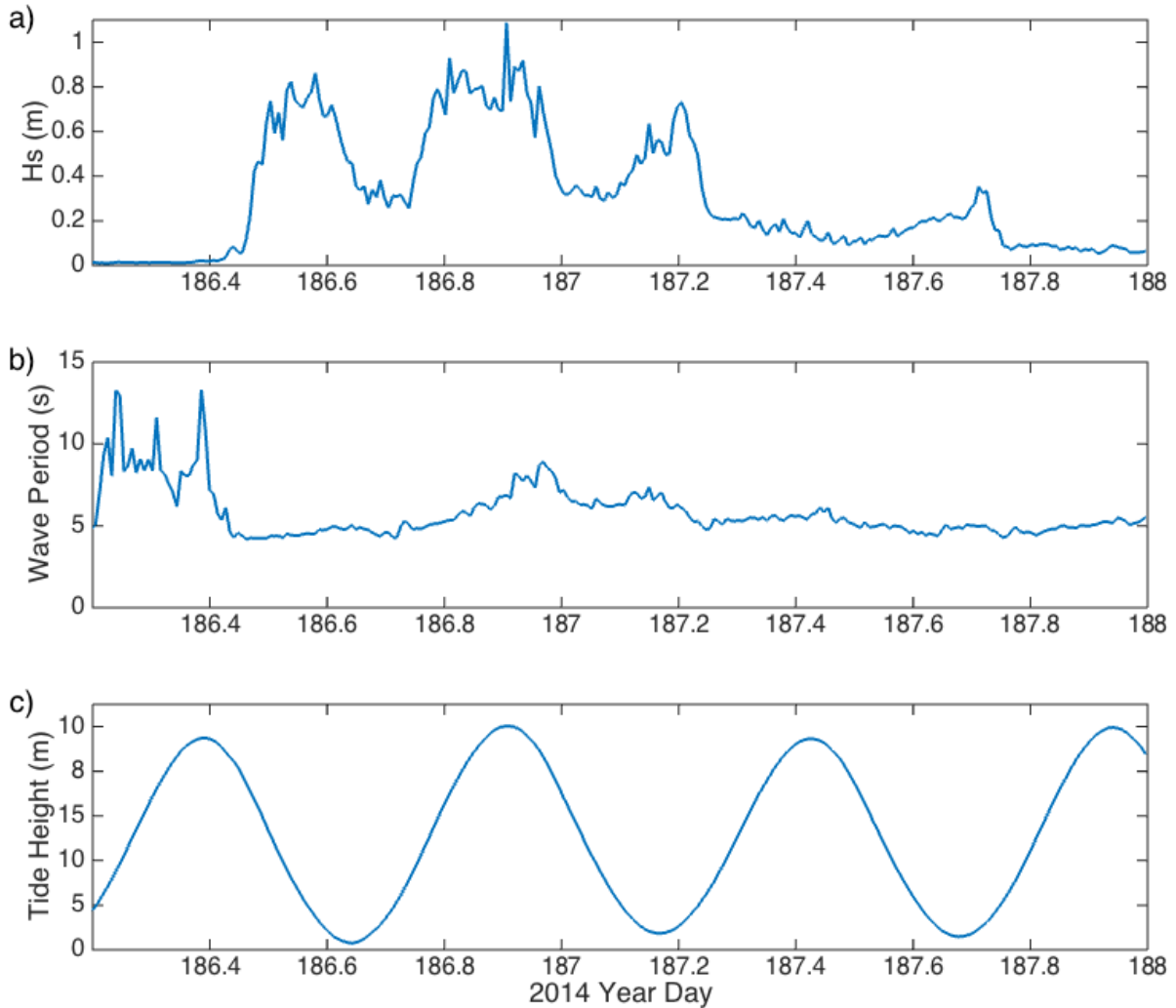
Figure 3.7 Wave conditions during PTS Arthur; a) wave heights, b) wave periods, and c) tide heights

3.4.2 Depth of Disturbance

The DOD values recorded following PTS Arthur on 8 July show a clear trend increasing landward, with greatest depth of 30.0 cm ± 0.4 cm at rod 5, decreasing to about 7.1 cm ± 0.4 cm at rod 2 (Fig. 3.8). A similar trend increasing landward is seen during calm conditions. Relative to the pre-storm beach surface, surveyed on 4 July, the day before the storm, accretion ($\Delta\eta > 0$) occurred at all the rod locations, with the low – 1 to 4 cm -- and comparable values at rods 1 to 3, whereas the values at rods 4 and 5 are much larger: 10 to 20 cm.
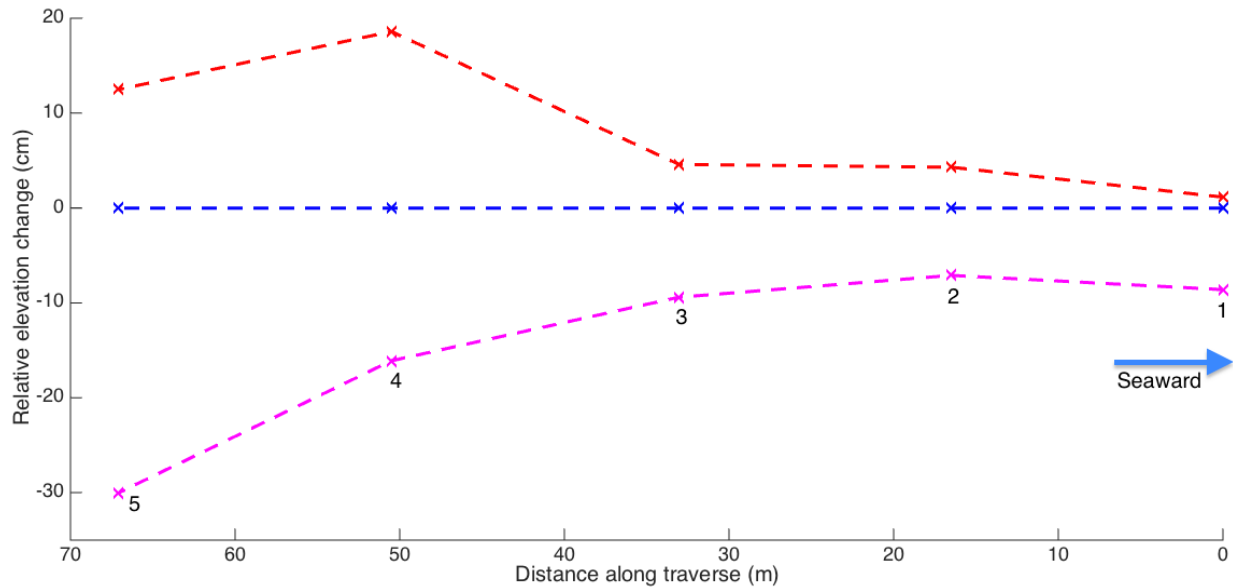
Figure 3.8 DOD (pink) and bed elevation change, $\Delta\eta$, (red) recorded post-Arthur (July 8th), relative to the pre-Arthur surface (July 4th) used as reference (blue)

3.4.3 Sediment Size Distribution Change

Rubin's (2004) spatial autocorrelation method was used to determine grain size distributions of the beach surface from photos taken along the rod array. Sediment distribution estimates show that the pre-Arthur surface had median grain size estimated at 30.3 mm and 23.3 mm using Rubin's (2004) original method and the cumulative sum method respectively. Median size estimates for post-Arthur show substantial fining: with the corresponding estimates being 17.2 mm and 14.1 mm. Examining the mean size distributions along the beach from the pre-Arthur surface and the post-Arthur surface, shown in Figures 3.9 and 3.10 respectively indicates how the sediment distribution has shifted. Sediments greater than 32 mm composed about half of the surficial sediment composition pre-storm. This fraction was reduced substantially to about one third and accordingly increased the finer fractions.
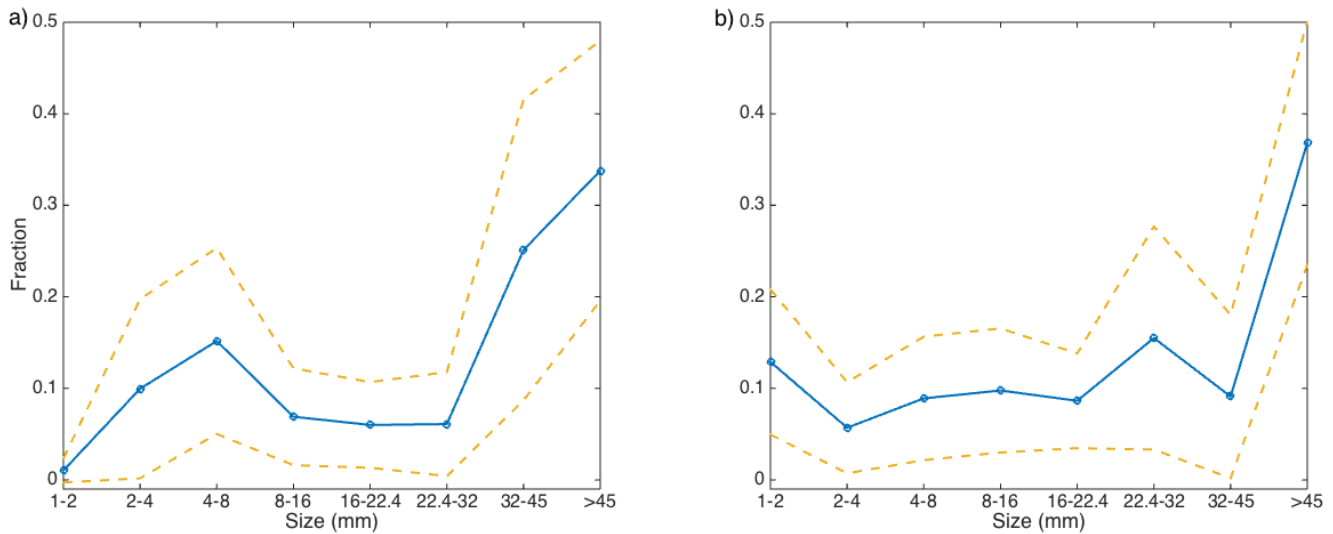
Figure 3.9. Pre-Arthur estimates of surficial sediment composition of the beach surface using Rubin's (2004) method (a) and the cumulative sum method (b)
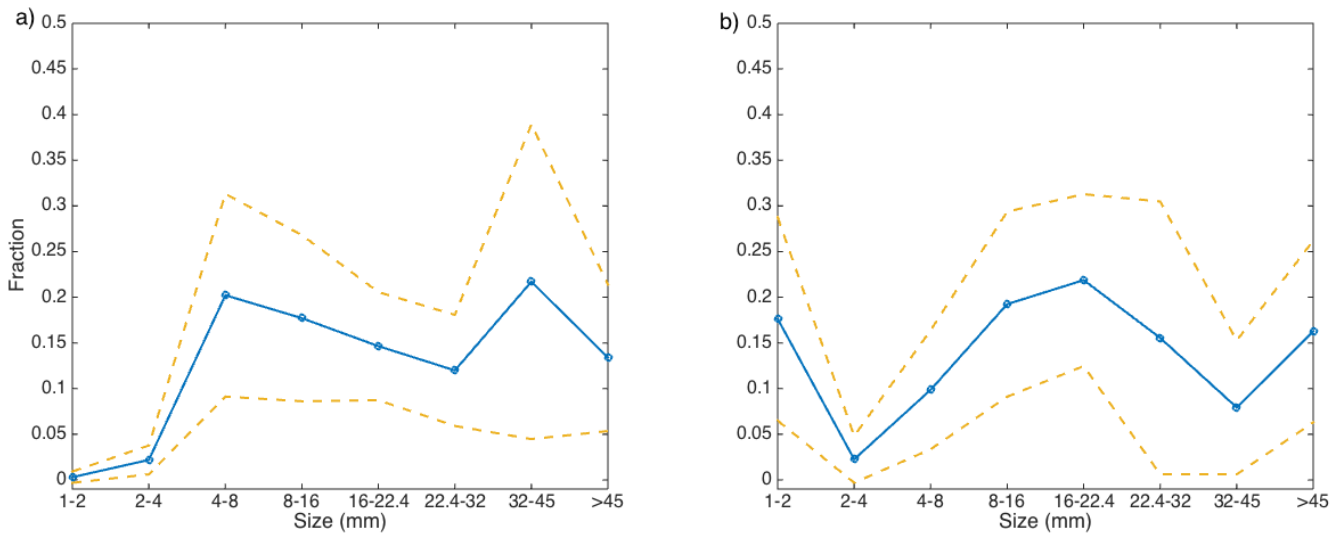
Figure 3.10. Post-Arthur estimates of surficial sediment composition of the beach surface using Rubin's (2004) method (a) and the cumulative sum method (b)

3.5 Beach Recovery

Continued study of the beach after the storm from 8 July (YD 189) to 5 September (YD 248) showed very little recovery relative to the pre-storm surface (Fig. 3.11). Relative beach elevation at rods 2 and 3 showed little change for the remainder of the study, at most deviating 2 cm from the post-storm surface, and then returning to the 8 July position upon rod removal on 5 September. Rods 4 and 5, with the highest levels of accretion, also showed little recovery relative to the pre-Arthur surface.

Rod 4 showed a consistent decrease in relative bed elevation, with the largest decrease just after the storm. Rod 5 showed continued increase after the storm until 25 July (YD 206) before decreasing. Rod 1, near low-water, was affected the least by PTS Arthur and stayed at about the same elevation until 5 September, when a 10-cm high shoreward-facing bedform migrated over the rod, increasing the bed elevation by about 10.4 cm $\pm$ 0.2 cm. Little change in D_{50} is observed after the initial fining post-Arthur, slight coarsening or fining may be possible (Fig. 3.12).
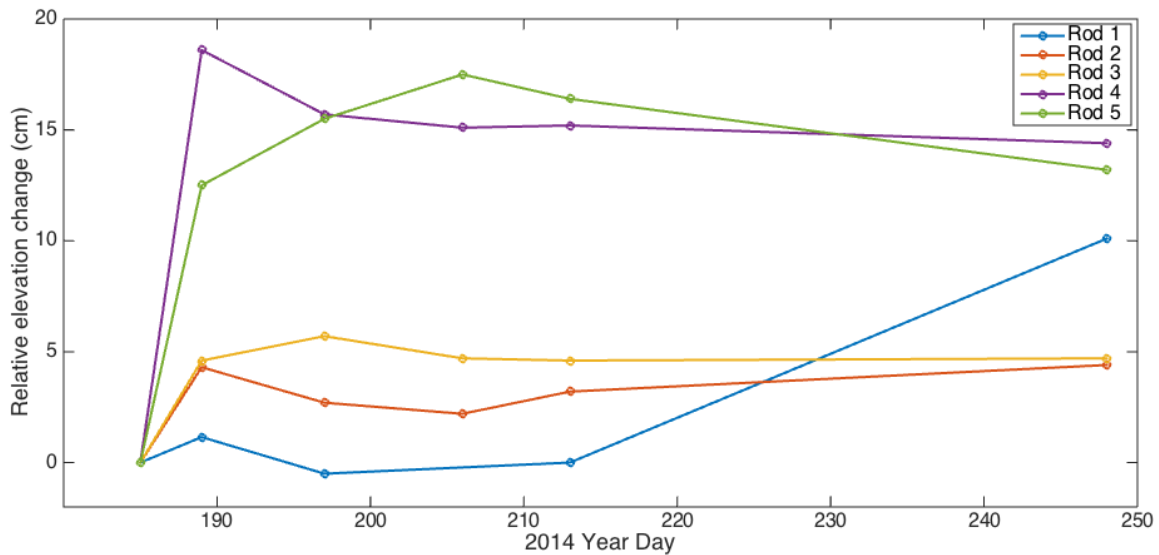
Figure 3.11 Time series of surface elevation change, $\Delta\eta$, at each rod relative to the pre-storm surface measured on July 4th (YD 185)
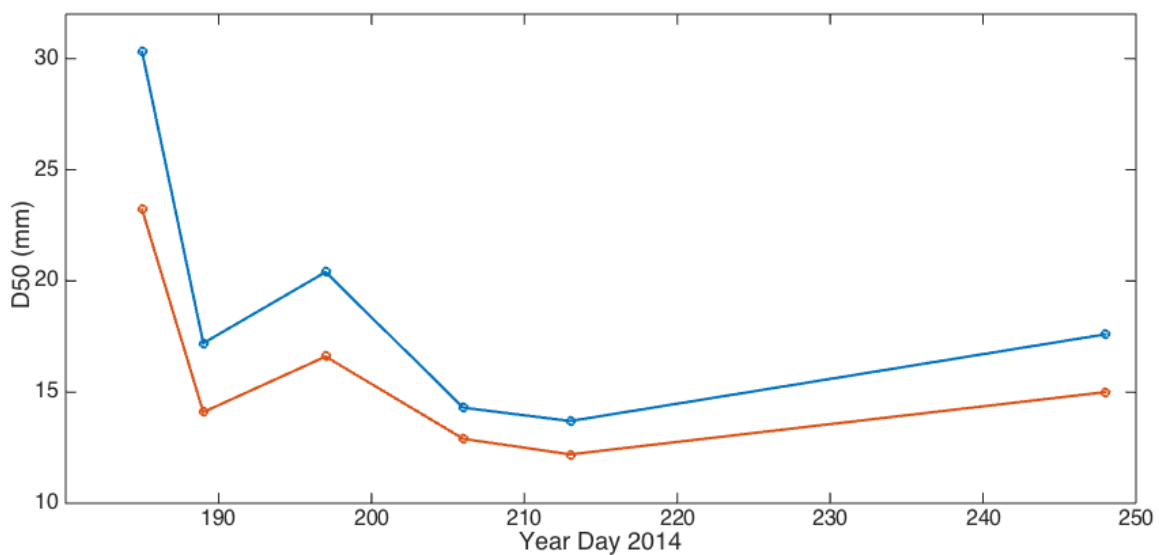
Figure 3.12 Time series of estimated beach surface D_{50} from photo surveys using Rubin's (2004) method (blue) and the cumulative sum method (red).3.6 A Curious Bedform

The bedform mentioned above in relation to the bed elevation change at Rod 1 is shown in the photographs in Figure 3.13 and 3.14. This feature persisted at the foot of the beach throughout the study. The crestline exhibited undulations of about 1 m in amplitude and 5-10 m wavelength, The feature is curious because it is the opposite of a shore-break step, which would have faced seaward.

Figure 3.13. The undulating nature of the curious bedform running along the shoreline. Notebook, 20 cm in length, as scale.

Figure 3.14. The steep landward slope of the curious bedform causing water to pool at low tide. Notebook for scale, 20 cm in length.

CHAPTER 4: DISCUSSION

4.1 Beach Classification

Jennings and Shulmeister (2002) classified mixed sand and gravel beaches as being composed of mixed sand and gravel through the profile, typically having an active profile slope (tanα) ranging from 0.05 to 0.14 and a D_{50} ranging from -1.65 to -5.21 φ. This classification, developed using beaches in New Zealand, is intended for micro- and mesotidal beaches, although it can be applied to our study site, a megatidal beach, successfully. Core samples show the vertical profile is composed of mixed sand and gravel, beach slope, with a tanα value of 0.1, and D_{50} of about -4 φ, fulfilling the proposed criteria corresponding to a MSG beach.

4.2 Wave Transformation

Wave transformation is important to understand because it governs the position of wave breaking, the primary control on DOD. It is clearly visible at BRB from processed wave data (Fig. 3.4 and Fig. 3.7). The wave shoaling effect, beach morphology, and tidal stage are the primary factors transforming waves at BRB.

Wave transformation by wave shoaling is recorded at the Dalhousie gauge installed at mid-beach (Fig. 3.4c). The effect produces maxima in wave heights as the tide recedes and approaches the mid-beach position, making a U-shape trend in wave heights as the tides oscillate above the gauge. This occurs because shoaling steepens waves as they approach shallower water. The pressure gauge is exposed to the shallowest water depths as tide rises and falls past it, resulting in higher waves recorded during these periods, as illustrated in Figure 4.1. The same effect also occurs at the FORCE gauge, installed about low tide, but is not as apparent because it is typically submerged except during spring tides.
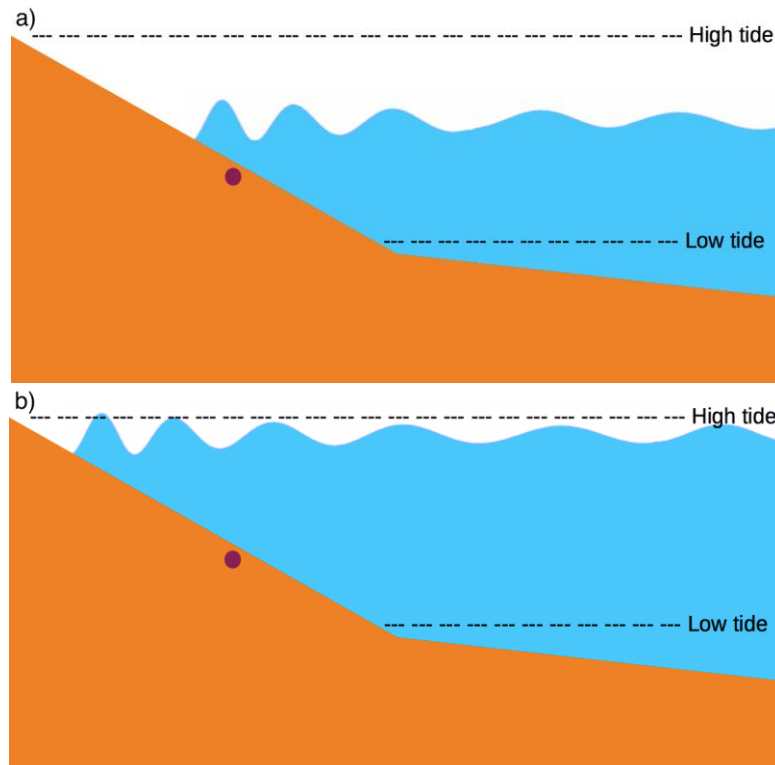
Figure 4.1 Wave shoaling effects resulting in different wave heights recorded at a pressure gauge at mid-tide marked in violet. a) Showing higher recorded wave heights as the tide recedes or approaches over the pressure gauge. b) Showing lower wave heights recorded over the pressure gauge at higher tidal stages.

The morphology of BRB, seen in Figure 1.3, is steep and planar, with a slope of 1:10 on the active profile and a much shallower slope of 1:30 just offshore beginning at about lowest low-water. Due to this steep, planar morphology waves are mostly free to propagate up and break on the beach face. However the large tidal range provides spatial and temporal control on wave breaking. Near low tide the waves are exposed to a much shallower beach slope of 1:30. The shallower slope causes waves to steepen and break farther from the shoreline. This prevents the energy of breaking waves from reworking the active beach about low tide, because the incoming wave energy is dissipated as the waves propagate over the shallow offshore-slope. The steeper 1:10 slope exposed during higher tidal stages allows wave breaking to occur closer to the shoreline. An approximate but oversimplified way of quantifying this to use the wave breaking criteria, the ratio of wave height to water depth, of 0.78 (Mei, 1989) to estimate the position of wave breaking. Using a wave height of 0.6 m, experienced during the

PTS Arthur, wave breaking would occur at about 23.6 m offshore from the water line at a depth of 0.77

m assuming a slope of 1:30, exposed at lower tidal stages. For a slope of 1:10, exposed at higher tidal

stages, wave breaking would occur just 7.7 m offshore from the water line. This effect is illustrated in

Figure 4.2.
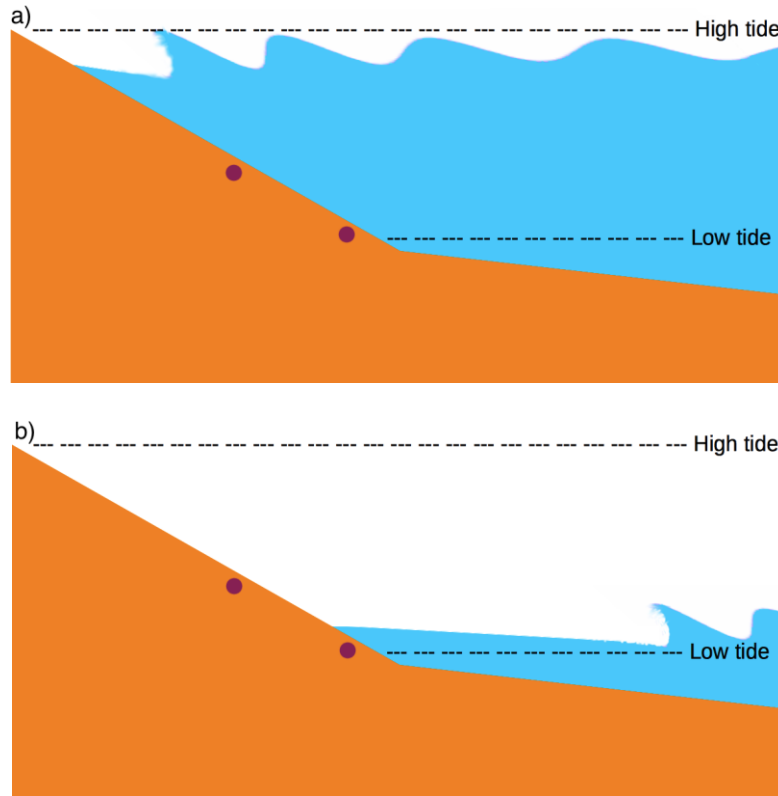
Figure 4.2 Position of wave breaking relative to the shoreline controlled by slope and tidal stage with
pressure gauge positions shown in violet. a) Waves exposed to the steeper slope of the active profile at
higher tidal stages allowing waves to break much closer to shore. b) Waves exposed to the shallower
offshore slope exposed at lower tidal stages, resulting in breaking farther from shore.

Morphology also provides a control on the amount of reworking that can occur by transforming

the type of wave breaking and in turn the amount of energy dissipated on the beach. As Beach and

Sternberg (1996) describe, plunging breakers dissipate a larger quantity of energy on the bed surface

compared to spilling breakers. Using the Iribarren number, ξ (Eq. 4.1), we can approximate the type of

wave breaking that will occur for the active and offshore profile (Battjes, 1974). The Iribarren number

is given by

$$\xi = \frac{tan\ \alpha}{\sqrt{H/L_o}} \tag{4.1}$$

where α is the angle of beach slope, H is the deep-water wave height, and L_0 is deep-water wavelength. There are two methods for calculating ξ, using deep-water heights or breaking wave heights. The wave heights collected for the study are about low-tide and are not true deep-water or breaking wave heights but lie somewhere in between. Using a wave height of 0.6 m and period of 6 s, conditions experienced during PTS Arthur, yields ξ values of 0.62 for the active slope (1:10) and 0.21 for the offshore slope (1:30). The ξ value for the active slope, 0.62, falls in the range for plunging breaker for both methods of calculating ξ, and the ξ value for the offshore slope of 0.21, falls in the range for spilling breakers also for both methods of calculation (Battjes, 1974). As described for wave breaking, tidal range also provides spatial and temporal control on breaker type because it changes the gradient to which the waves are exposed. Waves approaching at higher tidal stages will dissipate greater amounts of energy due to their plunging nature, whereas waves approaching at lower tidal stages dissipate less energy on the beach due to their spilling form.

Another way tides transform waves is through tidal currents. In offshore environments the effect of tidal currents are often negligible, however due to the large tidal range in the region and narrowed flow at Minas Passage tidal currents are significant enough to transform waves. This wave-current interaction is greatest during mid-tide, when current velocities are greatest. Evidence of this phenomenon at BRB is clearest in Figures 3.4a and 3.4b, where abrupt cyclical decreases in wave height occur with the change from flood to ebb tides. The abrupt change in wave heights suggests tidal currents reach maximum speed shortly after transitioning to between ebb and flood. The relative effects of wave-current interaction during PTS Arthur can be approximated by estimating phase speeds. Assuming the deep-water approximation to the dispersion relation, the phase speed c_p is given by

$$c_p = \frac{g}{\omega} \tag{4.2}$$

which, for 6 s period waves yields a value of about 10 m s^{-1}. Compared to maximum current speeds exceeding 5 m s^{-1} (Oceans LTD, 2009), it is clear that the currents will have a significant effect upon the trajectories of wave rays entering the Minas Passage from the Bay: i.e. the waves will be refracted by the shear in the tidal current as they traverse Minas Passage toward BRB.

The pattern of wave transformation during PTS Arthur (Fig. 3.7) is significantly different from patterns observed during calm conditions (Fig. 3.4). The patterns observed during calm conditions can be primarily attributed to tidal stage, where the change between ebb and flood tide coincides with an abrupt change in wave height. Patterns of transformation during PTS Arthur are not as simple but do show a similar pattern seen during calm conditions, with abrupt changes in wave height. However these abrupt changes in wave height do not completely coincide with the change between flood and ebb tides as seen during calm conditions. This increased complication can be partially explained with transformation due to beach morphology, which is temporally controlled by tidal stage interacting with transformation due to wave-current interaction. Transformation by beach morphology experienced during PTS Arthur has a much more significant effect due to much larger wave heights experienced compared to calm conditions. Wave heights during calm conditions were on the order of centimeters, whereas PTS Arthur generated waves up to a meter, allowing greater wave shoaling effects. The variability in wind speeds also helps to explain the variability in wave height, where the tallest wave heights occur just before and during the greatest wind speeds. Other factors affecting wave forcing, possibly relating to storm conditions may be unaccounted for.

4.3 Sediment Reworking

4.3.1 Depth of Disturbance

The trend seen in DOD post-Arthur, increased landward, with a maximum disturbance at rod 5, near high water. A simple explanation for this trend is the timing of waves and the tide. The highest

waves (*Hs* ~1 m) occurred at high tide (Fig. 3.7), exposing farther landward sections to more energetic conditions. From about mid-beach (rod 3) to low-water (rod 1), DOD is relatively consistent, at about 10 cm. This may be attributed to transformation by the shallower offshore slope causing spilling breakers to form instead of plunging and wave breaking to occur farther from the shoreline. However it is difficult to relate cross-shore differences in DOD to wave transformation directly with the present data set. Ideally, to examine effects of wave transformation, DOD measurements would be taken at each low tide during significant wave forcing events.

Ivamy and Kench (2006) reported the a cross-shore trend in DOD opposite to that observed here, increasing seaward instead of landward, on a MSG beach on Torere Bay, New Zealand. The seaward increase was attributed to the presence of a break-point step transforming incoming waves and the temporal control on transformation at the breakpoint step imposed by tides. About low-tide swell and steeper, more energetic wind waves break about the break-point step. Tide heights of about one third of high-water allowed shallower swell-waves to pass and propagate up shore whereas steeper wind-waves are still forced to break at the break-point step. This exposes higher sections of the beach to less wave energy, and in turn resulted in the seaward increasing trend of DOD. Similar processes of wave transformation also occur at BRB, however the increasing DOD landward can be primarily attributed to the difference in morphology. The steep, planar morphology of BRB, lacking a break-point step allows, for the most part, waves to propagate freely on to the beach. A maximum disturbance depth of 54 cm, reported by Ivamy and Kench (2006) about the break-point step, is much greater than the maximum recorded on BRB at 30 cm, however wave conditions were significantly different. Significant wave heights at BRB were much higher, ranging from 0.8 to 1.1 m, whereas on Torere Bay wave heights were about 0.5 m, indicating significant differences in energy dissipated through sediment reworking at both beaches. An important difference between the BRB and the Torere Bay beach is that the latter faces the open Pacific Ocean and is therefore subjected to continuous wave

action from Pacific swells. It is likely that this continuous action is at least partially responsible for the break-point step.

It is important to note that the sediment dynamics during wave action are not known because the high-energy environment limits instrumentation that can be installed. This leaves the possibility that maximum accretion may have occurred during wave action, which was subsequently removed or that higher levels of accretion during wave action may have also limited the maximum DOD observed. Another limitation to our study is the placement of DOD rods. The rods record an increasing trend landward indicating even higher DOD landward from our array. Ideally the array would have recorded a decline in DOD at some point. An improvement in future would be to extend the array farther landward.

4.3.2 Accretion

The general trend for DOD increasing landward is also present in the accreted portion however accretion peaks at rod 4, at the upper-mid-beach, just seaward of high water. Accretion was recorded along the length of the rod array post-Arthur (Fig. 3.8), indicating that the source of the accreted sediment is not along the study section. This leaves three possible sources, landward of our section about the storm berm, just offshore, and alongshore. A source alongshore is possible due to a longshore current brought about during wave action. Due to the geography of the BoF and Minas Passage, waves are limited to incident directions primarily from the east, generating a longshore current toward the southeast, following the trend of the shoreline. It is unlikely that the sediments are sourced from more landward sections of the beach due to the sheer volume accreted. Sediment sourced from either just offshore or along shore is more likely however without evidence for the sediment source the direction of transport cannot be determined. Understanding the source location is important because continued sediment removal from the same location could result in compounding degradation from successive

storms, potentially exposing buried cables. In addition to extending the array, noted earlier, adding parallel arrays along the shoreline would identify potential effects of longshore drift.

4.4 Surficial Sediment Composition

Sediment accretion and disturbance depths as a result of wave action during PTS Arthur indicate that the threshold of motion has been largely surpassed, particularly at upper portions of the beach where DOD are deepest. Fining of the beach was observed post-storm, with changes in D_{50} estimated at 30.3 mm and 23.3 mm to 17.2 mm and 14.1 mm using Rubin's (2004) original method and a the cumulative sum method respectively (Fig. 3.12). This fining as a result of energetic wave forcing matches observations made by Hay et al. (2014) at Advocate Beach on the BoF, similar in morphology and composition to BRB. As Hay et al. (2014) mention, the result is counter-intuitive as finer material is typically removed during initial stages of storm wave action and during winter storm season.

Sediment compositions of MSG beaches are usually coarser at surface, containing more gravel with sands filling the interstitial spaces (Horn and Walton, 2007). Wave action resulting in mixing of generally finer sediment at depth is likely the cause of observed fining for surficial sediments directly after energetic wave action resulting from PTS Arthur. This explanation is supported by the median grain size of 16.0 mm interpolated from the surficial sediment sample taken pre-storm to 7 cm depth, which is in the range of median grain sizes of the beach post-Arthur. To account for coarser surficial sediment composition observed pre-Arthur, more long-term processes are probably at play. A possible explanation is that threshold of motion for the finer fractions is being met during calm conditions, allowing something similar to the Brazil nut effect to take place, where finer material is allowed to fall through the interstitial spaces between the larger grains resulting in gradual coarsening of the surface. The shallow DOD, a few centimeters in scale during calm conditions may work to enhance this effect. Offshore or alongshore transport of finer material are also possible explanation of the observed fining.

CHAPTER 5: CONCLUSION

5.1 Summary

PTS Arthur, representative of the most powerful storms to make landfall in the region, generated significant wave heights of up to 1.1 m. A trend of DOD increasing landward was recorded post-Arthur, with 30.0 cm ± 0.4 cm recorded at the farthest landward position and 7.1 cm ± 0.4 cm recorded at the most seaward position of the rod array. Along the entire length of the array accretion was recorded, raising a question with regard to the source for the accreted sediment, a question which could not be addressed in this study because of the limitations of the 1-dimensional DOD array. Rubin's (2004) method, using SAC, was modified to process larger images and estimate sand fractions more reliably. Using this method significant fining of the beach face was recorded post-Arthur, opposite of what is typically expected after storm-wave action. Wave transformation, governed by beach slope and tidal stage, provide spatial and temporal controls on wave breaking and amount of energy dissipated through sediment reworking. Due to the infrequent occurrence of storms on the scale of Arthur it is difficult to relate wave transformation directly to the pattern of waves recorded, however the effects of wave transformation during calm conditions are more easily understood. Even with these gaps in knowledge and limitations in study design a cable burial depth can be recommended following an increasing landward trend at depths at least double the DOD observed post-Arthur.

5.2 Further Research

Several questions were left unanswered by this study. The source of sediment accreted along the traverse is not known, leaving three possible sources, offshore, landward, and along shore from the rod array. The increasing trend of DOD landward, with a maximum at the most landward rod, indicates even greater disturbance depths beyond the range of the rod array. An improvement addressing both of

these problems would be to extend to rod array landward and seaward and to install parallel arrays along shore. The relationship between DOD and wave transformation is unclear because PTS Arthur was the only significant wave event and persisted longer than a single tidal cycle. A way to improve understanding of this relationship is to improve temporal resolution by taking DOD measurements between each tidal cycle at low tide during significant wave action. Continuing the photo survey of the beach surface and increasing the sampling interval can also improve understanding change in surficial sediment composition. Capturing more wave events and extending the study period to examine seasonal changes in forcing, especially in the winter with the effects of ice would be the best next step in understanding MSG beach dynamics in the BoF.

REFERENCES

Anfuso, G. (2005). Sediment-activation depth values for gentle and steep beaches. *Marine Geology*, 220(1), 101-112.

Battjes, J. A. (1974). Surf similarity. Coastal Engineering Proceedings, 1(14).

Beach, R. A., & Sternberg, R. W. (1996). Suspended-sediment transport in the surf zone: response to breaking waves. *Continental Shelf Research*, 16(15), 1989 2003.

Ciavola, P., Taborda, R., & Ferreira, Ó. (1997). Field observations of sand-mixing depths on steep beaches. *Marine Geology*, 141(1), 147-156.

Greenwood, B., & Hale, P. B. (1980). Depth of activity, sediment flux, and morphological change in a barred nearshore environment.

Horn, D. P., & Walton, S. M. (2007). Spatial and temporal variations of sediment size on a mixed sand and gravel beach. *Sedimentary Geology*, 202(3), 509-528.

Hay, A. E., Zedel, L., & Stark, N. (2014). Sediment dynamics on a steep, megatidal, mixed sand gravel–cobble beach. *Earth Surface Dynamics*, 2(2), 443-453.

Ivamy, M. C., & Kench, P. S. (2006). Hydrodynamics and morphological adjustment of a mixed sand and gravel beach, Torere, Bay of Plenty, New Zealand. *Marine Geology*, 228(1), 137-152.

Jennings, R., & Shulmeister, J. (2002). A field based classification scheme for gravel beaches. *Marine Geology*, 186(3), 211-228.

Keppie, J.D (compiler). Geological Map of Nova Scotia. 1:500,000. Nova Scotia: Geological Survey of Canada Nova Scotia Department of Natural Resources, Minerals and Energy, 2000

King, C. A. M. (1951). Depth of disturbance of sand on sea beaches by waves. *Journal of Sedimentary Research*, 21(3).

Mason, T., & Coates, T. T. (2001). Sediment transport processes on mixed beaches: a review for shoreline management. *Journal of Coastal Research*, 645-657.

McKay, P. J., & Terich, T. A. (1992). Gravel barrier morphology: Olympic National Park, Washington State, USA. Journal of Coastal Research, 813-829.

Mei, C. C. (1989). Currents Induced by Breaking Waves. In *Advanced series of ocean engineering: The applied dynamics of ocean surface waves* (p. 467). Singapore: World Scientific.

Oceans LTD. (2009, May). Currents in Minas Basin. Hansport, Canada: Minas Basin Pulp and Power.

O'Reilly, C.T., Solvason, R. and Solomon, C. (2005). "Where are the World's Largest Tides?" BIO Annual Report "2004 in Review", Editor Judith Ryan, ISBN:0-662 40330-4, pp 44-46.

Parrott, D. R., Todd, B. J., Shaw, J., Hughes Clarke, J. E., Griffin, J., MacGowan, B. & Webster, T. (2008). Integration of multibeam bathymetry and LiDAR surveys of the Bay of Fundy, Canada. In *Proceedings of the Canadian Hydrographic Conference and National Surveyors Conference* (pp. 6-2).

Quick, M. C., & Dyksterhuis, P. (1994). Cross-shore transport for beaches of mixed sand and gravel. In *International Symposium: Waves—Physical and Numerical Modeling*. Canadian Society of Civil Engineers (pp. 1443-1452).

Rubin, D. M. (2004). A simple autocorrelation algorithm for determining grain size from digital images of sediment. *Journal of Sedimentary Research*, 74(1), 160-165.

Saini, S., Jackson, N. L., & Nordstrom, K. F. (2009). Depth of activation on a mixed sediment beach. *Coastal Engineering*, 56(7), 788-791.

Withjack, M. O., Olsen, P. E., & Schlische, R. W. (1995). Tectonic evolution of the Fundy rift basin, Canada: evidence of extension and shortening during passive margin development. *Tectonics*, 14(2), 390-405.

APPENDIX A: DATA TABLES

Table 1. DOD rod data for July 8th

	July 8th (YD189)		
DDR #	Hi (cm)	Ha (cm)	Hd (cm)
1	47.2 ± 0.2	46.0 ± 0.2	55.8 ± 0.2
2	44.0 ± 0.2	39.7 ± 0.2	51.1 ± 0.2
3	42.2 ± 0.2	37.6 ± 0.2	51.6 ± 0.2
4	38.7 ± 0.2	20.1 ± 0.2	54.8 ± 0.2
5	39.5 ± 0.2	27.0 ± 0.2	69.5 ± 0.2

Table 2. DOD rod data for July 16th

	July 16th (YD 197)		
DDR #	Hi (cm)	Ha (cm)	Hd (cm)
1	46.7 ± 0.2	47.7 ± 0.2	47.7 ± 0.2
2	40.7 ± 0.2	41.3 ± 0.2	41.3 ± 0.2
3	38.1 ± 0.2	36.5 ±0.1	39 ± 0.2
4	20.2 ± 0.2	23.0 ± 0.2	25 ± 0.2
5	26.6 ± 0.2	24 ± 0.5	28.9 ± 0.2

Table 3. DOD rod data for July 25th

	July 25th (YD 237)		
DDR #	Hi (cm)	Ha (cm)	Hd (cm)
1	47.7 ± 0.2	tide too high	tide too high
2	41.3 ± 0.2	41.8 ± 0.2	41.8 ± 0.2
3	36.0 ± 0.2	37.5 ± 0.2	38.2 ± 0.2
4	22.4 ± 0.2	23.6 ± 0.2	25.6 ± 0.2
5	24 ± 0.2	22 ± 0.2	26.7 ± 0.2

Table 4. DOD rod data for August 1st

	August 1st (YD 213)		
DDR #	Hi (cm)	Ha (cm)	Hd (cm)
1	tide too high	47.2 ± 0.2	47.2 ± 0.2
2	41.8 ± 0.2	40.8 ± 0.2	42.7 ± 0.2
3	37.3 ± 0.2	37.6 ± 0.2	38.2 ± 0.2
4	23.3 ± 0.2	23.5 ± 0.2	27.4 ± 0.2
5	26.0 ± 0.2	27.1 ± 0.2	29.3 ± 0.2

Table 5. DOD rod data for September 5th

	September 5th (YD 244)		
DDR #	Hi (cm)	Ha (cm)	Hd (cm)
1	47.2 ± 0.2	37.1 ± 0.2	47.5 ± 1
2	39.6 ± 0.2	39.6 ± 0.2	45 ± 0.5
3	37 ± 0.2	37.5 ± 0.2	39.8 ± 0.2
4	23 ± 0.2	24.3 ± 0.2	28.5 ± 0.2
5	26.9 ± 0.2	30.3 ± 0.2	32.4 ± 0.2